PNAS RESEARCH ARTICLE | BIOPHYSICS AND COMPUTATIONAL BIOLOGY OPEN ACCESS

# Spontaneous nucleation and fast aggregate-dependent proliferation of α-synuclein aggregates within liquid condensates at neutral pH

Samuel T. Dada[a], Maarten C. Hardenberg[a], Zenon Toprakcioglu[a], Lena K. Mrugalla[a], Mariana P. Cali[a,b], Mollie O. McKeon[a], Ewa Klimont[a], Thomas C. T. Michaels[a,c,d], Tuomas P. J. Knowles[a], and Michele Vendruscolo[a,1]

Edited by William Eaton, National Institute of Diabetes and Digestive and Kidney Diseases, Bethesda, MD; received May 22, 2022; accepted January 1, 2023

**The aggregation of α-synuclein into amyloid fibrils has been under scrutiny in recent years because of its association with Parkinson's disease. This process can be triggered by a lipid-dependent nucleation process, and the resulting aggregates can proliferate through secondary nucleation under acidic pH conditions. It has also been recently reported that the aggregation of α-synuclein may follow an alternative pathway, which takes place within dense liquid condensates formed through phase separation. The microscopic mechanism of this process, however, remains to be clarified. Here, we used fluorescence-based assays to enable a kinetic analysis of the microscopic steps underlying the aggregation process of α-synuclein within liquid condensates. Our analysis shows that at pH 7.4, this process starts with spontaneous primary nucleation followed by rapid aggregate-dependent proliferation. Our results thus reveal the microscopic mechanism of α-synuclein aggregation within condensates through the accurate quantification of the kinetic rate constants for the appearance and proliferation of α-synuclein aggregates at physiological pH.**

phase separation | protein condensates | Parkinson's disease

Parkinson's disease is the most common neurodegenerative movement disorder (1, 2). A distinctive pathophysiological signature of this disease is the presence of abnormal intraneuronal protein deposits known as Lewy bodies (3, 4). One of the main components of Lewy bodies is α-synuclein (5), a peripheral membrane protein highly abundant at neuronal synapses (6, 7) and genetically linked with Parkinson's disease (8, 9). This 140-residue disordered protein can be subdivided into three domains, an amphipathic N-terminal region (amino acids 1 to 60), a central hydrophobic region (non-amyloid-β component, or NAC, amino acids 61 to 95), and an acidic proline-rich C-terminal tail (amino acids 96 to 140) (7). Although α-synuclein aggregation is characteristic of Parkinson's disease and related synucleinopathies, the corresponding mechanism and its possible pathological role in disease are not yet fully understood.

Generally, the aggregation process of proteins proceeds through a series of interconnected microscopic steps, including primary nucleation, elongation, and secondary nucleation (10, 11). During primary nucleation, the self-assembly of proteins from their native, monomeric form leads to the formation of oligomeric species, an event that may occur in solution or on surfaces including biological membranes (12, 13). The formation of these oligomers is typically a slow event governed by high kinetic barriers (10, 11). Once formed, the oligomers may convert into ordered assemblies rich in β structure, which are capable of further growth into fibrillar aggregates (14). In many cases, the surfaces of existing fibrillar aggregates then further catalyze the formation of new oligomers (15, 16). This secondary nucleation process is typically characterized by the assembly of protein monomers on the surface of fibrils that eventually nucleate into new oligomeric species (15, 16). This autocatalytic mechanism generates rapid fibril proliferation (15).

In the case of the aggregation process of α-synuclein, several key questions are still open, including two that we are addressing in this study. The first concerns whether there are cellular conditions under which α-synuclein can undergo spontaneous aggregation, and the second whether the proliferation of α-synuclein fibrils by aggregate-dependent feedback processes can take place at physiological pH. These questions are relevant because according to our current knowledge, α-synuclein aggregation does not readily take place spontaneously in the absence of contributing factors such as lipid membranes. Furthermore, secondary nucleation contributes significantly to the aggregation process only at acidic pH (13, 17). It thus remains challenging to rationalize the links between α-synuclein aggregation and Parkinson's disease.

## Significance

It has been recently shown that the speed of the conversion of α-synuclein from its native state into amyloid fibrils can be greatly enhanced by the formation of an intermediate dense liquid state formed through phase separation. The corresponding mechanism, however, remains to be fully characterized. In this work, we use a combination of fluorescence microscopy, microfluidics, and chemical kinetics to determine the microscopic rate constants for the primary nucleation and aggregate-dependent proliferation at neutral pH of α-synuclein fibrils. The approach that we report facilitates the study of the aggregation process of α-synuclein under physiological conditions and of its relationship with Parkinson's disease and related synucleinopathies.

Author contributions: S.T.D. and M.V. designed research; S.T.D., Z.T., M.P.C., T.C.T.M., and M.V. performed research; S.T.D., M.C.H., Z.T., L.K.M., M.O.M., E.K., T.C.T.M., T.P.J.K., and M.V. contributed new reagents/analytic tools; S.T.D., M.C.H., Z.T., L.K.M., M.O.M., E.K., T.C.T.M., T.P.J.K., and M.V. analyzed data; and S.T.D., M.C.H., Z.T., L.K.M., M.P.C., M.O.M., E.K., T.C.T.M., T.P.J.K., and M.V. wrote the paper.

The authors declare no competing interest.

This article is a PNAS Direct Submission.



[1]To whom correspondence may be addressed. Email: mv245@cam.ac.uk.

This article contains supporting information online at https://www.pnas.org/lookup/suppl/doi:10.1073/pnas.2208792120/-/DCSupplemental.

Published February 21, 2023.

To address this problem, we investigated whether it is possible to leverage the recent finding that α-synuclein can undergo a phase separation process resulting in the formation of dense liquid condensates (18–21). Phase separation has recently emerged as a general phenomenon associated with a wide variety of cellular functions (22–25) and closely linked with human disease (23, 26–29). This process has been reported for a wide range of proteins implicated in neurodegenerative conditions, including tau, fused in sarcoma (FUS), and TAR DNA binding protein 43 (TDP-43) (30–32). Since it has also been shown that protein aggregation can take place within liquid condensates (19, 26, 32–36), we asked whether it is possible to characterize at the microscopic level the condensate-induced aggregation mechanism of α-synuclein by determining the kinetic rate constants of the corresponding microscopic processes.

To enable the accurate determination of the rate constants for the microscopic steps in α-synuclein aggregation within condensates, we developed fluorescence-based aggregation assays to monitor both the spontaneous aggregation of α-synuclein and the aggregation in the presence of aggregate seeds. Using these assays within the framework of a kinetic theory of protein aggregation (10, 11, 37), we show that α-synuclein can undergo spontaneous homogenous primary nucleation and fast aggregate-dependent proliferation within condensates at physiological pH.

## Results and Discussion

**Prerequisites for the Study of α-Synuclein Aggregation Following Phase Separation.** Increasing evidence indicates that aberrant protein aggregation can take place within dense liquid condensates generated through phase separation (18, 19, 21, 26, 32–35). Fluorescence recovery after photobleaching can be employed to monitor the progressive maturation of the liquid condensates (38), and the subsequent appearance of solid-like assemblies (18, 19) (*SI Appendix*, Fig. S1 and Movies S1 and S2). The accurate time-dependent measurement of the formation of ordered aggregate species, however, is still challenging. Therefore, the study of α-synuclein aggregation within condensates requires the development of a strategy to capture the initial stages of phase separation, the maturation of the resulting condensates, as well as the key microscopic steps that drive the subsequent conversion into amyloid aggregates.

**An In Vitro Strategy for the Study of α-Synuclein Aggregation within Liquid Condensates.** To monitor closely the microscopic steps that drive α-synuclein aggregation within liquid condensates, we built on an established assay based on confocal microscopy used to observe rapid phase separation of α-synuclein in vitro (19). This assay enables the monitoring of α-synuclein condensates over time and is conducted by depositing a small sample volume as a droplet on a microscopy slide, where the phase separation process can be observed at physiological pH through the use of a molecular crowding agent, in our case polyethylene glycol (PEG) (Fig. 1 and *SI Appendix*, Fig. S2 *A–D*). Phase separation of α-synuclein can subsequently be characterized in real-time with fluorescence microscopy using a confocal microscope and α-synuclein labeled with Alexa Fluor 647. Next, to obtain a robust readout of the conversion of α-synuclein from its monomeric state to the amyloid state, we implemented the use of thioflavin T (ThT), a well-known benzothiazole fluorescent amyloid-binding dye employed for in vitro and in vivo characterization of amyloid formation (10, 19) (*SI Appendix*, Fig. S2*E*). ThT exhibits an enhanced fluorescent signal upon binding the cross-β structures characteristic of amyloid fibrils (10, 19). Our results indicate that ThT is soluble in PEG at the experimental conditions used in this work and can respond to changes in concentration of preformed α-synuclein fibrils (*SI Appendix*, Fig. S3).

We then aimed to investigate the ability of ThT to detect fibrillar species formed within α-synuclein condensates (Fig. 1 and Movie S3). To this end, monomeric α-synuclein labeled with the fluorophore Alexa Fluor 647 was incubated in the presence of 20 μM ThT and observed for about 20 min (Fig. 1*A*). This timeframe was chosen based on the observation that condensates transition from a liquid to a solid state about 20 min after the onset of phase separation (*SI Appendix*, Figs. S1 and S4). We observed a general increase in ThT fluorescence over time at various concentrations of α-synuclein, suggesting that fibrillar species had formed within the condensate (Fig. 1 *B–D*). During the first few minutes from the start of the phase separation process, the vast majority of α-synuclein was present in its monomeric state (Fig. 1 *B* and *C*). After 10 min, a notable increase in ThT emission was detected (Fig. 1 *B* and *C*), as evidenced by an exponential growth phase, which is indicative of a rapid increase in cross-β α-synuclein species within condensates (39). Such a speedy amplification of aggregate mass points toward the presence of secondary pathways, driving the amplification of cross-β aggregates (10, 11, 39). After approximately 18 min, the ThT emission reached a plateau, as most monomeric α-synuclein had been converted into fibrils (Fig. 1 *B* and *C*), indicating completion of the aggregation process.

To characterize their morphology at the end point of the assay, we performed transmission electron microscopy (TEM) imaging 24 min post the onset of phase separation. As expected, the TEM images indicated that α-synuclein fibrils had indeed formed. No fibrillar structures were observed prior to phase separation, and when individual components of the assay were assessed individually (*SI Appendix*, Fig. S5 *A* and *B*). Circular dichroism spectroscopy was employed to confirm the disordered, monomeric structure of α-synuclein prior to the observation of condensates. Fourier-transform infrared spectroscopy (FTIR) was then employed to characterize the structure of the amyloid aggregates formed pre and post phase separation (40, 41) (*SI Appendix*, Fig. S5 *C–E*). From the second derivative FTIR spectra, the prominent bands at 1,629 $cm^{-1}$ and 1,627 $cm^{-1}$ are indicative of β-sheet secondary structure composition (42) (*SI Appendix*, Fig. S5*E*). Taken together, the enhancement of ThT fluorescence, the observed fibrillar structures by TEM and prominent β-sheet infrared absorbance, which are all consistent with amyloid fibril formation, indicate that our assay is capable of monitoring the formation of α-synuclein fibrils following phase separation.

**The ThT-Based Aggregation Assay Is Sensitive to Changes in Phase Separation Behavior.** As phase separation has been reported to depend on low-affinity electrostatic and hydrophobic interactions (43, 44), we used this feature to test the sensitivity of the aggregation assay described above in detecting changes in the protein interactions governing phase separation. A salt, sodium chloride (NaCl), and an aliphatic alcohol, 1,6-hexanediol, were chosen as controls due to their wide applications as effective tools to probe the material properties of protein condensates and inclusions (19, 45). NaCl alters the electrostatic interactions between protein molecules in the phase separation process, while 1,6-hexanediol works by interfering with the weak hydrophobic interactions that promote the formation of protein condensates. As expected, 1,6-hexanediol had a concentration-dependent inhibitory effect on the formation of α-synuclein condensates (Fig. 2 *A–C*). On the other hand, an increase in ionic strength led to a higher amyloid fibrillar yield (Fig. 2 *A*, *D*, and *E*), a result that implicates the involvement of the acidic C-terminal region

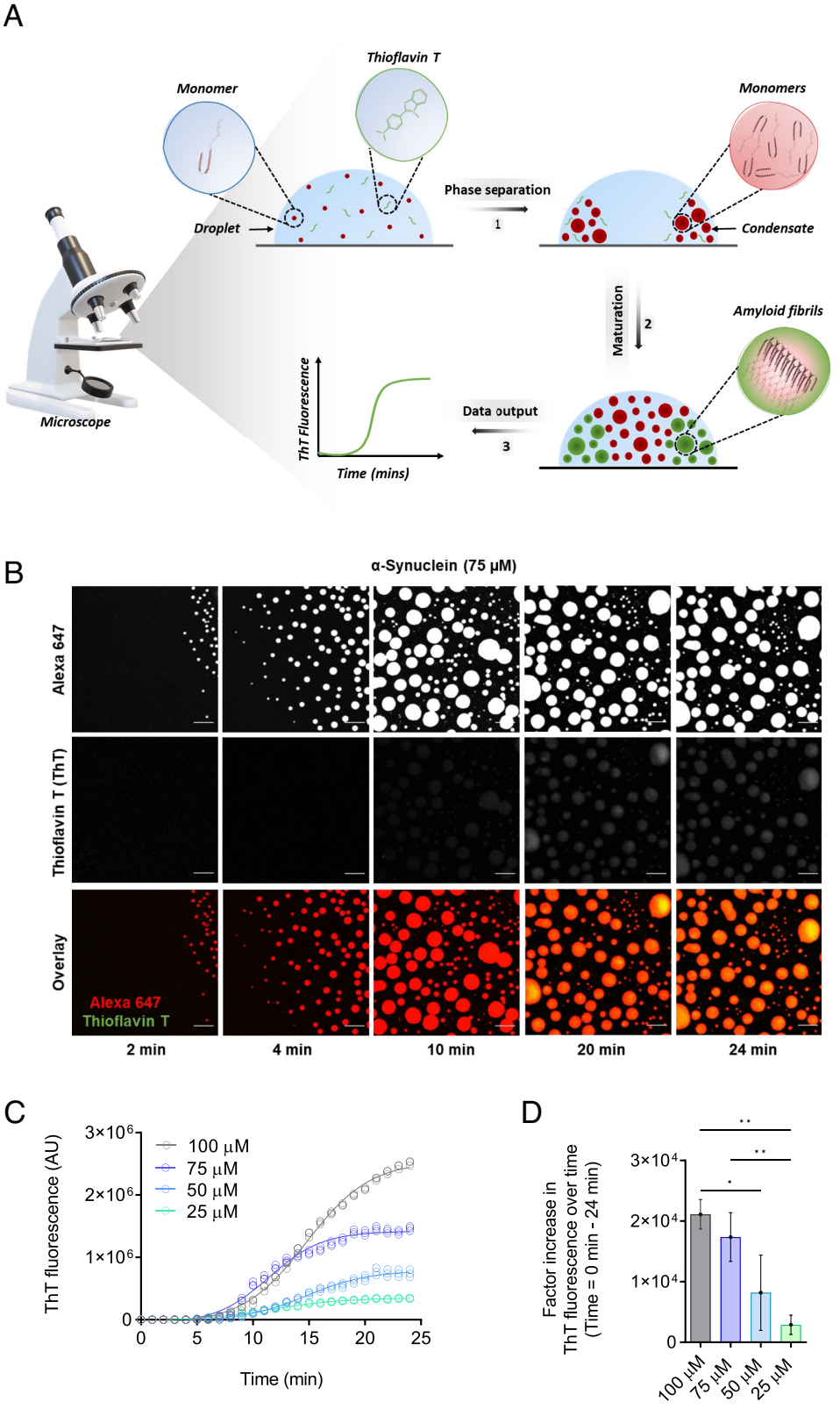


**Fig. 1.** Development of a ThT-based assay to monitor α-synuclein aggregation within liquid condensates. (*A*) The assay has three components: 1) the phase separation of α-synuclein into dense liquid droplets (condensates) within dilute liquid droplets, which is monitored using Alexa Fluor 647 fluorescence, 2) the formation of α-synuclein amyloid fibrils over time within the condensates, and 3) the real-time assessment of amyloid formation is performed using ThT fluorescence. (*B*) Imaging of α-synuclein condensate formation (using Alexa Fluor 647 fluorescence) and aggregation (using ThT fluorescence) over time. In the presence of a crowding agent (10% PEG), α-synuclein monomers (75 μM) form a dense liquid phase surrounded by a dilute liquid phase. In the presence of 20 μM ThT, amyloid-containing condensates can be detected as an increase in the ThT fluorescence signal over time. The images represent an area of the sample that was tracked over time. (The scale bar represents 10 μm.) (*C*) Quantification of ThT fluorescence over time of the images shown in panel *B* for 75 μM (blue) α-synuclein. Subsequently, ThT emission for 100 (gray), 50 (cyan), and 25 (turquoise) μM α-synuclein were obtained in the same manner over 24 min. (*D*) Factor increase in ThT fluorescence intensities across the different concentrations tested (the ThT intensity at 24 min was subtracted by the ThT intensity at 0 min divided by the ThT intensity at 0 min). All experiments were performed in 50 mM Tris-HCl at pH 7.4 in the presence of 10% PEG and 20 μM ThT. The data represent the mean ± SEM of n = 3 individual experiments. One-way ANOVA., $*P < 0.1$, $**P < 0.01$.

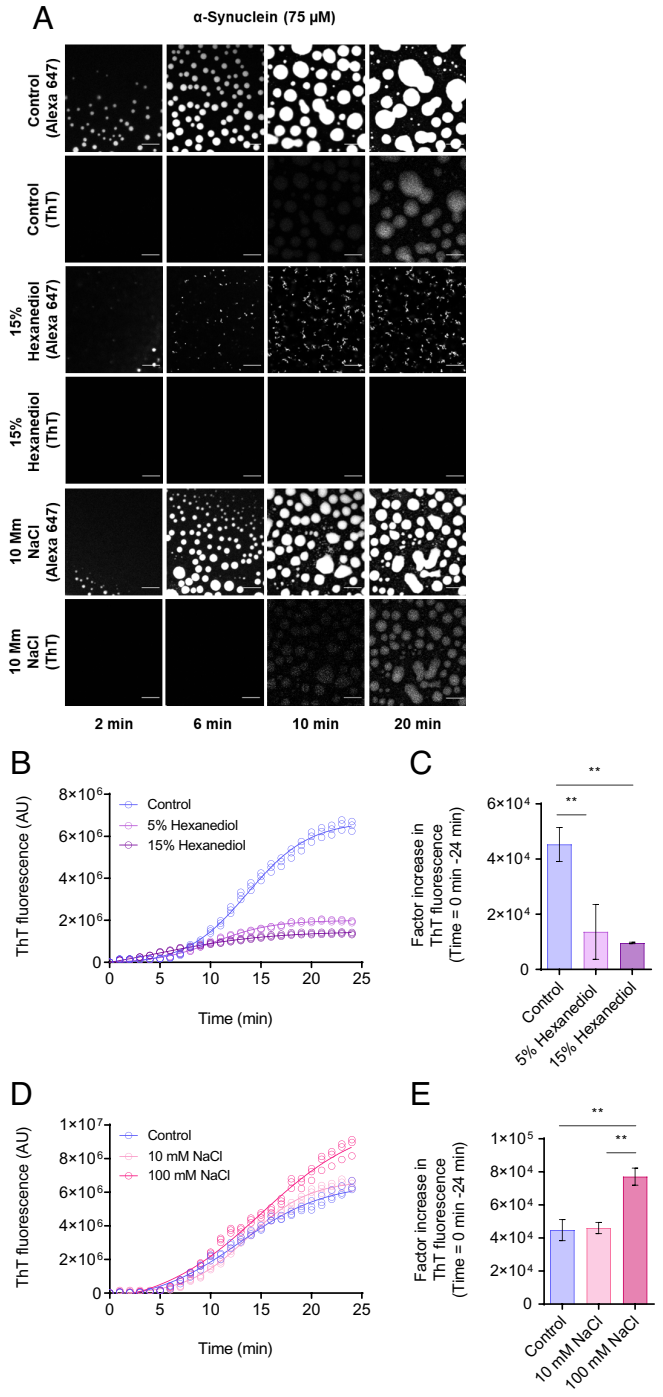


**Fig. 2.** The ThT-based aggregation assay is sensitive to changes in the phase separation behavior. (*A*) Fluorescent images showing α-synuclein condensate formation (using Alexa Fluor 647 fluorescence) and aggregation (using ThT fluorescence) in the presence and absence (control) of 1,6-hexanediol (15% w/v), and 100 mM NaCl. The images suggest that the assay is sensitive to changes in the interactions between α-synuclein monomers as a result of 1,6-hexandiol and NaCl. (The scale bars represent 10 μm.) The images displayed represent an area of the droplet that was tracked over time. (*B*) Quantification of the ThT emission over time for the images shown in panel *A* for 75 μM α-synuclein (control) (blue) in the presence of 15% (w/v) (dark purple) and 5% (w/v) (light purple) 1,6-hexanediol over a 24-min period. (*C*) Factor increase in ThT fluorescence intensities from the data in panel *B* (the ThT intensity at 24 min was subtracted by the ThT intensity at 0 min divided by the ThT intensity at 0 min). (*D*) Rate of α-synuclein aggregation for the images in panel *A* in the presence and absence (blue) of 10 mM (light pink) and 100 mM (pink) NaCl over a 24-min period. (*E*) Factor increase in ThT fluorescence intensities from data in panel *D* (the ThT intensity at 24 min was subtracted by the ThT intensity at 0 min divided by the ThT intensity at 0 min). All experiments were performed using 75 μM α-synuclein in 50 mM Tris-HCl at pH 7.4 in the presence of 10% PEG and 20 μM ThT. The data represent mean ± SEM of n = 3 individual experiments. One-way ANOVA., *$P < 0.1$, **$P < 0.01$

of α-synuclein in its phase behavior. Taken together, these results demonstrate a reliable method of assessing α-synuclein aggregation within dense liquid condensates.

**A Framework to Elucidate the Mechanism of α-Synuclein Aggregation within Condensates.** Using the assay described above, we aimed to unravel the kinetic mechanisms by which monomeric α-synuclein transitions into fibrillar aggregates within liquid condensates. We first set out to establish a model of α-synuclein aggregation within condensates in an unperturbed system. Using the web-based software AmyloFit, we can characterize the complex reaction networks associated with protein aggregation using experimentally obtained kinetic data (39).

Our data show that there is only a weak dependence of the aggregation kinetics on the total monomer concentration. This behavior is fundamentally different from that observed commonly for amyloid solution in dilute solution, where the nucleation and elongation steps are controlled by reaction rates that depend on the monomer concentration. By contrast, here, when the aggregation reaction takes place within a phase separated system, the local concentration within the condensed phase does not depend on the total protein concentration, the latter quantity only affecting the fraction of the system that is found in the condensed state (Fig. 3 and *SI Appendix*, Fig. S6 *A* and *B*).

This conclusion was further verified through monitoring the critical concentration for phase separation. To this effect, we used a microfluidic device, which trapped protein-containing aqueous microdroplets. In this way, we eliminated possible effects of the slide surface on the phase separation process in the confocal microscopy assay described above. By monitoring the microdroplets over time and by shrinking them in a controlled manner (*SI Appendix*, Fig. S6*C*), hence increasing the protein concentrations, we estimated the concentration of α-synuclein required for phase separation (Fig. 3 *A*–*C*). We observed that the concentration required for phase separation is independent of the initial protein concentration, but rather depends on the crowding agent (*SI Appendix*, Fig. S6 *D* and *E*). This observation could explain why a concentration-dependent effect cannot be observed in the kinetics, as we study the maturation of α-synuclein once phase separation is observed.

We then determined the monomeric protein concentration within the condensates as a function of time and of the monomeric protein concentration in the dilute phase. The fluorescence intensity of Alexa Fluor 647 was used as readout for monomeric protein concentrations, as this accounts for 1% (molar) of the total α-synuclein concentration (Fig. 3 *D*–*F*). We observed that the monomeric protein concentration within condensates, 6 min post phase separation did not change despite an increase in amyloid formation (*SI Appendix*, Fig. S6*F*). As condensates mature and grow in a concentration-dependent manner, we wanted to establish whether there was a correlation between the condensate size and the monomeric concentration of α-synuclein in the dense phase. At all tested concentrations, there was a weak correlation between these variables, and the differences of spread of data between concentrations were not significant (*SI Appendix*, Figs. S6*F* and S7). Given these results, we then estimated the concentration of labeled α-synuclein in the condensates to be around 300 to 400 μM. Since just 1% of α-synuclein was labeled, this result indicates that the total concentration of α-synuclein in the condensates is about 30 to 40 mM for all initial α-synuclein concentrations tested (400, 100, 75, and 50 μM). This estimate was done using a previously described method where the fluorescence intensity of individual α-synuclein condensates was measured, and Alexa Fluor 647 was used to make

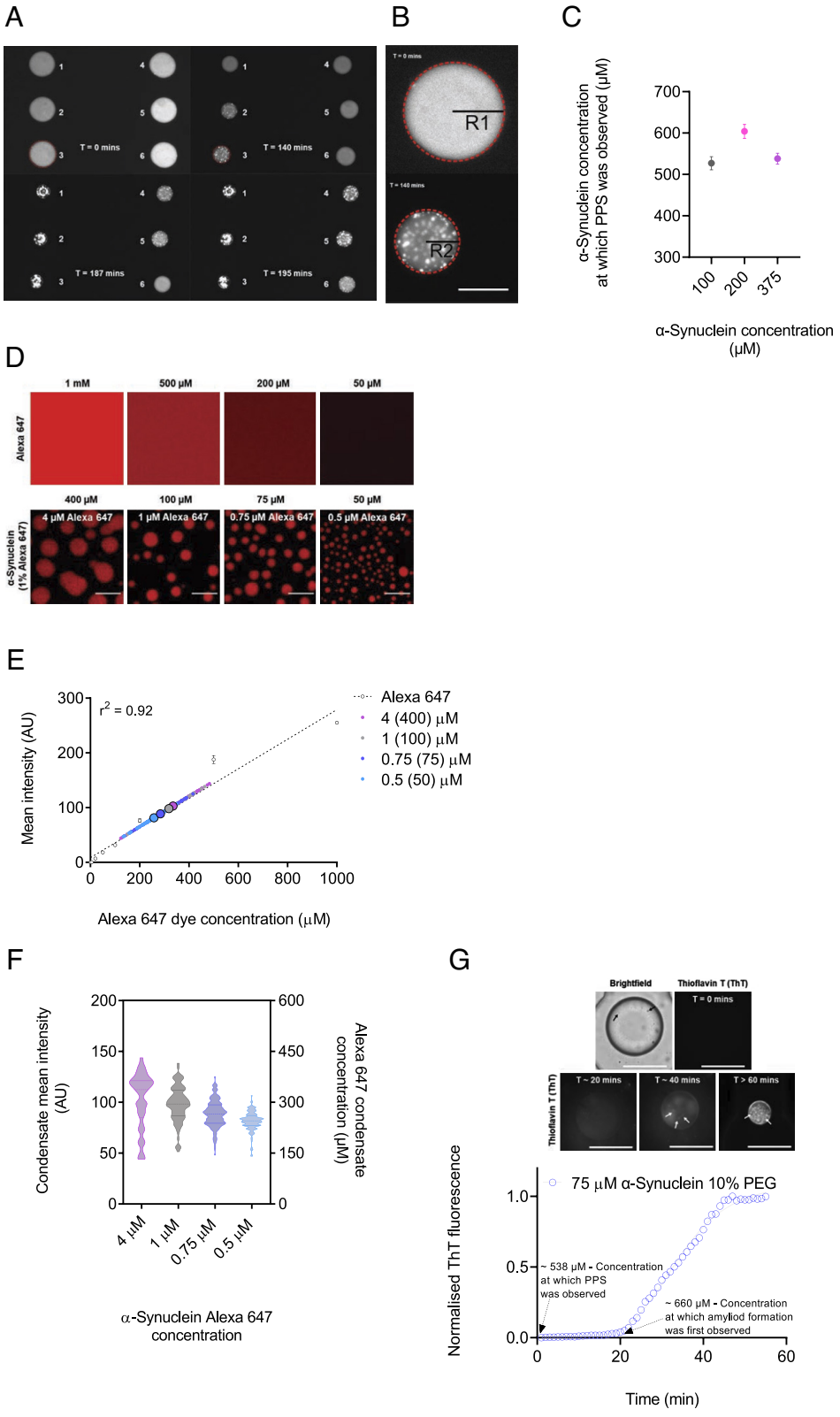


**Fig. 3.** The aggregation kinetics of α-synuclein within condensates show a weak concentration dependence. Within condensates, normalized aggregation data at four α-synuclein concentrations (100, 75, 50, and 25 μM), yielded almost no variations between different concentrations (*SI Appendix*, Fig. S5 *A* and *B*). (*A*–*C*) The concentration required for phase separation of α-synuclein was obtained using a microfluidic device. (*A*) Representative fluorescence images displaying the timeline of condensate formation within several droplets (assigned a number from 1 to 6) trapped within a microfluidic chamber at 0, 140, 187, and 195 min (Movie S4). (*B*) Magnified image from panel *C* showing a droplet at the start (0 min) of the experiment and following initiation of phase separation (140 min). The concentration required for phase separation is obtained from the initial protein concentration and the change in droplet radius from the start (R1) of monitoring the droplet to the point at which phase separation is observed (R2). (The scale bar represents 50 μm.) (*C*) α-Synuclein concentration at which phase separation was observed within droplets as shown in panels *C* and *D*, at different initial protein concentrations (100 (gray), 200 (pink), and 100 (purple) μM) in the presence of 10% PEG, was calculated to be an average of 527, 604, and 538 μM, respectively (*SI Appendix*, Table S1). (*D*) Fluorescence images of Alexa Fluor 647 at a range of concentrations (1,000, 500, 200, and 50 μM) and images of monomeric α-synuclein (400, 100, 75, and 50 μM) condensates 10 min from the onset of phase separation. (The scale bar represents 10 μm.) (*E*) Fluorescence intensity of Alexa Fluor 647 from at a range of 1 to 1,000 μM from images shown in panel *D* was used to obtain a calibration curve of fluorescence signal for calibration (linear regression, $r^2$ = 0.92). Small circles are the individual condensates measured for each α-synuclein concentration (n > 70 condensates per concentration), and big circles indicate the mean α-synuclein condensate intensity for each concentration [400 (light purple), 100 (gray), 75 (blue), and 50 (cyan) μM, and 4, 1, 0.75, and 0.5 μM for their respective 1% Alexa Fluor 647 protein concentration]. (*F*) Quantification of the mean fluorescence intensity (left Y axis) for individual condensates at each α-synuclein Alexa Fluor 647 concentrations 10 min from the onset of phase separation, and concentration within liquid droplets of α-synuclein labeled with Alexa Fluor 647 (right Y axis) at a range of bulk concentrations (400, 100, 75, and 50 μM) was estimated to be 335 ± 98, 319 ± 64, 284 ± 48 and 258 ± 34 μM after 10 min from the onset of phase separation (n > 70 condensates per concentration). (*G*) The concentration at which amyloid formation of α-synuclein was observed using a microfluidic device. Representative fluorescence images displaying the timeline of amyloid formation within droplet (75 μM α-synuclein, 10% PEG and 20 μM ThT) trapped within a microfluidic chamber at 0, 20, 40, and >60 min post protein phase separation (PPS). The α-synuclein concentration at which phase separation was observed within droplets was calculated to be an average of 538 ± 15.9 μM, and the concentration within droplet at which amyloid formation was observed was calculated to be an average of 660 ± 21.4 μM. (The scale bar represents 50 μm.) Data are shown for a representative experiment that was repeated at least three times.

a calibration curve for fluorescence intensity (36) (Fig. 3 *D*–*F* and *SI Appendix*, Fig. S6*H*). Thus, the estimated total concentration of α-synuclein in condensates is about three orders of magnitude higher than in the diluted phase. The observation with respect to the lack of any significant difference in the variation in protein concentration within the condensates across all tested concentrations can be described by the phenomenon known as concentration buffering, which exist in phases separation of binary solutions, where variation in protein concentration in the bulk phase is buffered by the phase separated compartments (46, 47). Therefore, droplets with higher protein concentrations form larger condensates, whereas droplets with lower protein concentrations form smaller condensates (*SI Appendix*, Figs. S4*A* and S6*G*). Using the microfluids device

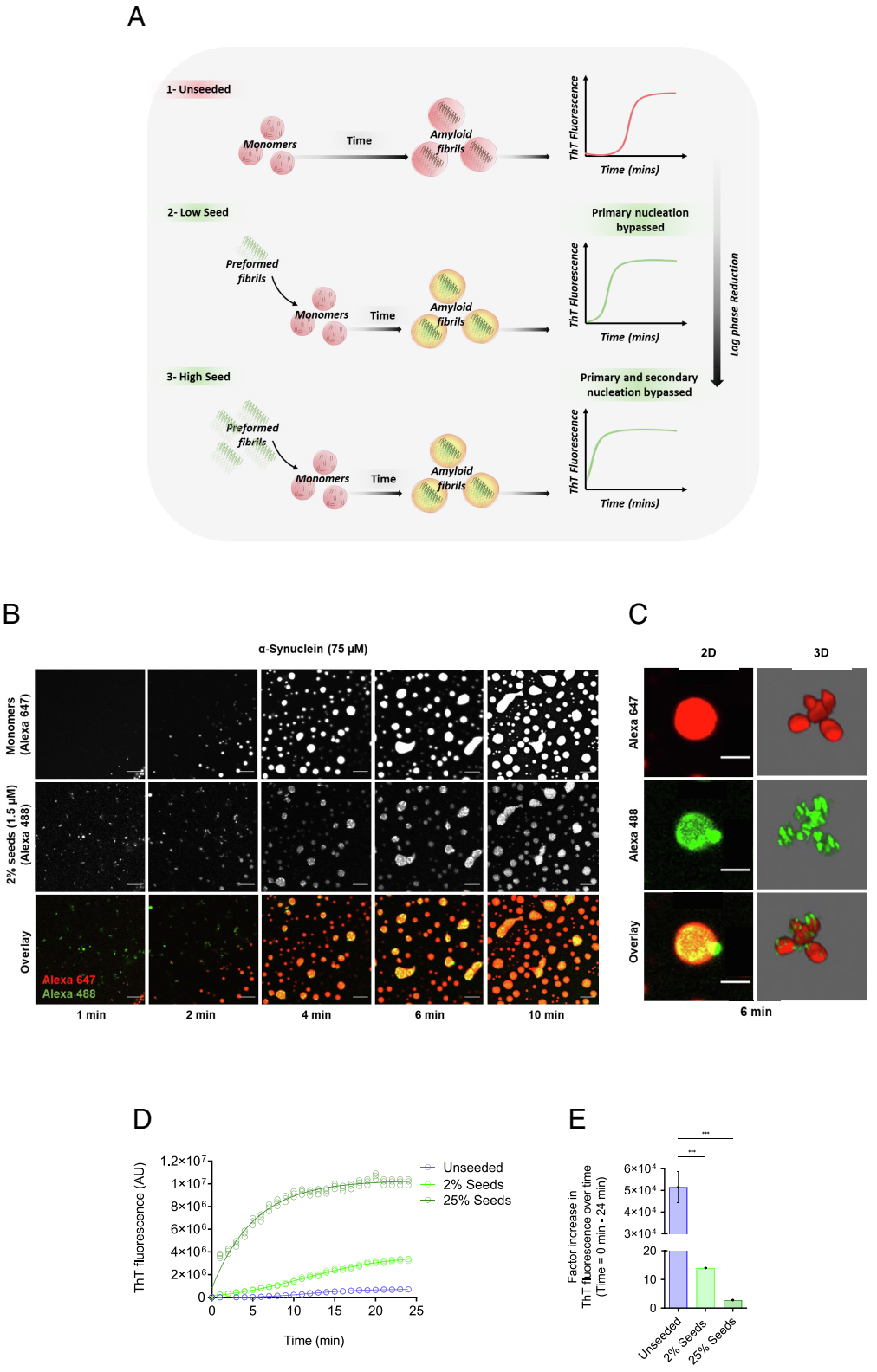


**Fig. 4.** The addition preformed α-synuclein fibrils bypasses the primary nucleation of α-synuclein within condensates. (*A*) Schematic diagram illustrating the seeding process within the condensates. In the presence of preformed fibrils (seeds), aggregation is accelerated (2 and 3), whereas in the absence of seeds aggregation is slower (1). Increasing seed concentration results in a reduced lag time. (*B*) Representative fluorescence imaging displaying condensate formation by α-synuclein monomer (75 μM, labeled with Alexa Fluor 647) in the presence of 2% (1.5 μM) preformed α-synuclein fibrils (labeled with Alexa Fluor 488), 10% PEG in 50 mM Tris-HCl (pH 7.4). At 1 min, the presence of preformed fibrils within the droplet is observed in the dilute liquid phase. Upon the formation of droplets, preformed fibrils are seen to colocalize with condensates thereby accelerating aggregation by propelling the formation of aggregates. The images represent an area of the sample that was tracked over time. (The scale bar represents 10 μm.) (*C*) 2D and 3D rendered images of different droplets showing that preformed fibrils (labeled with Alexa Fluor 488) are directly recruited into α-synuclein condensates (labeled with Alexa Fluor 647) (Movie S5). (The scale bar represents 10 μm.) (*D*) Progression of ThT emission as a function of time (24 min) for 75 μM α-synuclein monomers (unseeded) (blue) with the addition of 2% (1.5 μM) (light green) and 25% (18.75 μM) (dark green) preformed fibrils. The data report on the increase in the ThT signal over time (unseeded, 2% seeds, 25% seeds). (*E*) Relative increase in the raw data values of the ThT fluorescence intensities from time from the onset of phase separation to 24 min post it. All aggregation assays were performed in 50 mM Tris-HCl (pH 7.4) in the presence of 10% PEG and 20 μM ThT. The results are shown as mean ± SEM. One-way ANOVA; ***$P \leq 0.001$.

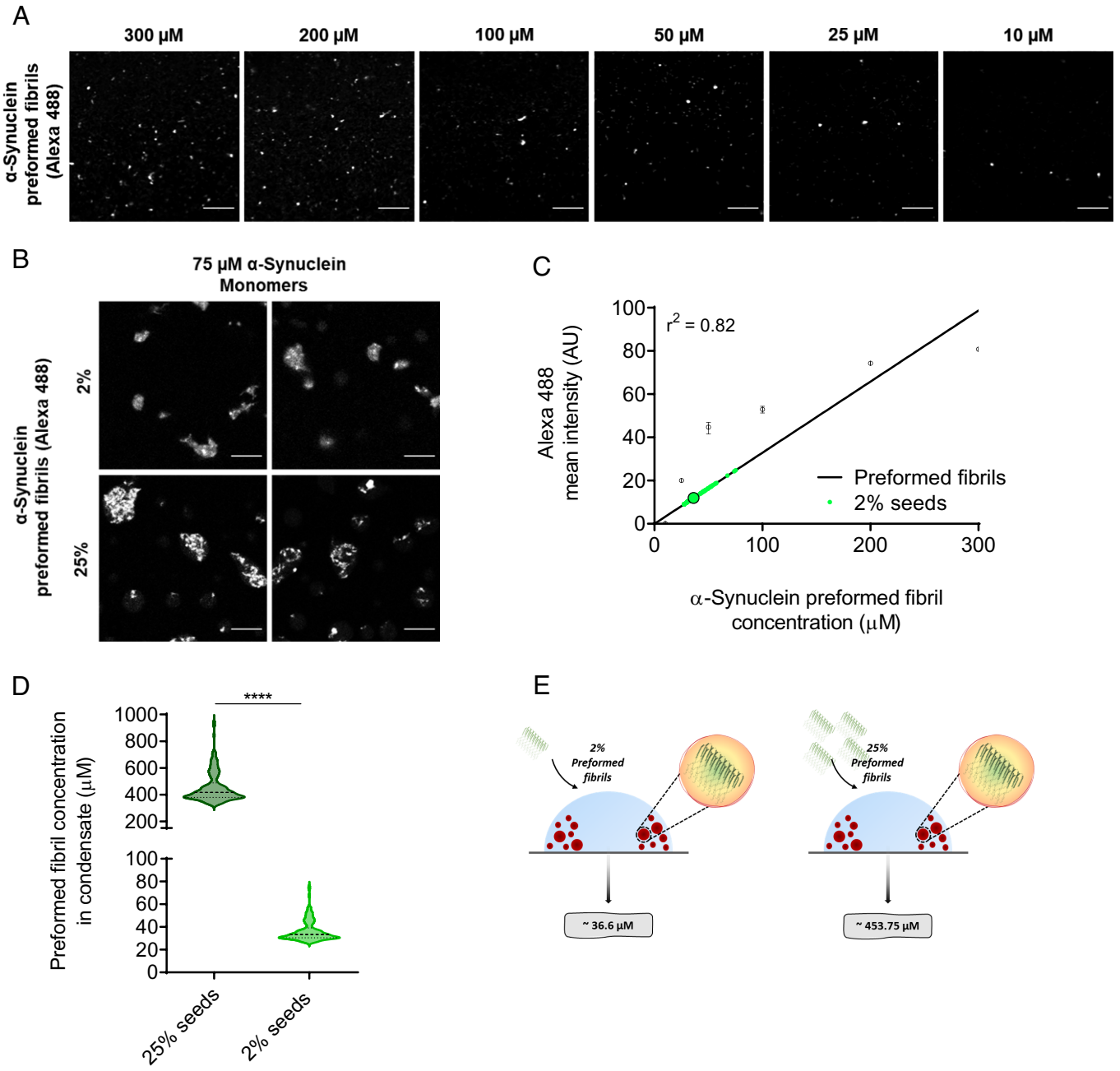


**Fig. 5.** Determination of the concentration of preformed α-synuclein fibrils within α-synuclein condensates. (*A*) Fluorescence images of preformed α-synuclein fibrils (labeled with Alexa Fluor 488) at decreasing concentrations (300, 200, 100, 50, 25, and 10 μM). (The scale bar represents 10 μm.) (*B*) Representative fluorescence imaging displaying colocalization of 2% and 25% preformed fibrils (labeled with Alexa Fluor 488) within α-synuclein condensates (labeled with Alexa Fluor 647) 10 min post phase separation. (The scale bar represents 10 μm.) (*C*) The data reported in panel *A* were used for the calibration of the Alexa Fluor 488 fluorescence signal (linear regression, $r^2 = 0.82$). The small circles are the individual condensates (n > 100) measured 10 min from the onset of phase separation and the big circle indicates the mean intensity of all fluorescently labeled preformed α-synuclein fibril within condensates. The Alexa Fluor 488 fluorescence signal of condensates in the assay containing 25% preformed fibrils had a higher intensity than the intensity of 300 μM preformed fibrils used for the calibration curve. (*D*) The average concentration of 2% (1.5 μM) and 25% (18.75 μM) preformed α-synuclein fibrils (labeled with Alexa Fluor 488) within α-synuclein condensates (75 μM) was estimated as 36 μM (SD = ±9, Min = 27, Max = 75 μM) and 454 μM (SD = ±112, Min = 341, Max = 939 μM), respectively. The results refer to 10 min from the onset of phase separation (n > 100 condensates). (*E*) Schematic illustrating the total concentration of preformed α-synuclein fibrils within condensates to be approximately 36.3 and 453.75 μM for 2% and 25% seeds, respectively. Data are from a representative experiment repeated three times with similar results. All seeded aggregation experiments were performed in 50 mM Tris-HCl (pH 7.4) and 10% PEG. The results are shown as mean ± SEM. One-way ANOVA; ****$P \leq 0.0001$.

described above, we also obtained the concentration at which amyloid formation was first observed in the droplets, which are shrinking during the experiments (Fig. 3*G*).

**Secondary Processes Dominate α-Synuclein Aggregation within Condensates.** We next investigated the role of aggregate-dependent secondary processes on α-synuclein aggregation within condensates. The addition of preformed α-synuclein fibrils at the beginning of the aggregation assay is typically used as a qualitative way to check for the presence of secondary processes, as they act as seeds to aid in aggregate growth and multiplication (39). On these grounds, we aimed to bypass primary nucleation (with rate constant $k_n$) events by adding a small amount of seeds (2%), where the rate of fibril formation is driven by secondary nucleation (with rate constant $k_2$),

fragmentation (with rate constant $k_-$), and elongation (with rate constant $k_+$) (15). The addition of large amounts (25%) of preformed seeds leads to primary and secondary nucleation being bypassed, and elongation of the preformed fibrils becoming the dominant process of aggregation (15) (Fig. 4*A*). If secondary processes are indeed present in α-synuclein aggregation within condensates, we expect a shortening in the lag phase in the presence of the preformed fibrils (Fig. 4*A*). Upon phase separation, preformed fibrils were observed to colocalize with the condensates, thus speeding up amyloid formation (Fig. 4 *B* and *C* and Movie S5).

Our results indicate that α-synuclein aggregation within condensates was accelerated in the presence of seeds as most newly formed fibrils were generated through secondary processes (Fig. 4*D*). In the presence of 25% preformed fibrils, α-synuclein aggregation was accelerated drastically to the extent that the plateau phase was reached 10 min post phase separation (Fig. 4 *D* and *E*). Visually, the presence of preformed fibrils within our assay was observed prior to phase separation (Fig. 4*B*). Overall, the data suggest that secondary processes are involved in the aggregation of α-synuclein within condensates. To confirm this result, we calculated the concentration of preformed fibrils within the condensates.

To estimate the concentration of preformed α-synuclein fibrils within condensates, several condensates containing fluorescently labeled preformed fibrils were assessed for their fibril content from several time points between 6 and 20 min (Fig. 5). We estimated the concentration of preformed α-synuclein fibrils within condensates to be 37 μM for 2% seeds (1.5 μM). We obtained this result by monitoring the intensity of individual α-synuclein condensates (formed from an initial concentration of 75 μM monomeric α-synuclein) containing preformed fibrils, and using a range of Alexa Fluor 488 fibril concentrations (50 to 300 μM) to create a calibration curve of Alexa Fluor 488 mean fluorescence intensity (Fig. 5 *A*–*D*). With regard to 25% seeds (18.75 μM), the average mean fluorescence intensity was greater than that of the highest concentration (300 μM) used for the calibration curve (Fig. 5*C*). In view of this, the equation $c^I \cong 24.2c^{tot}$ was derived to estimate

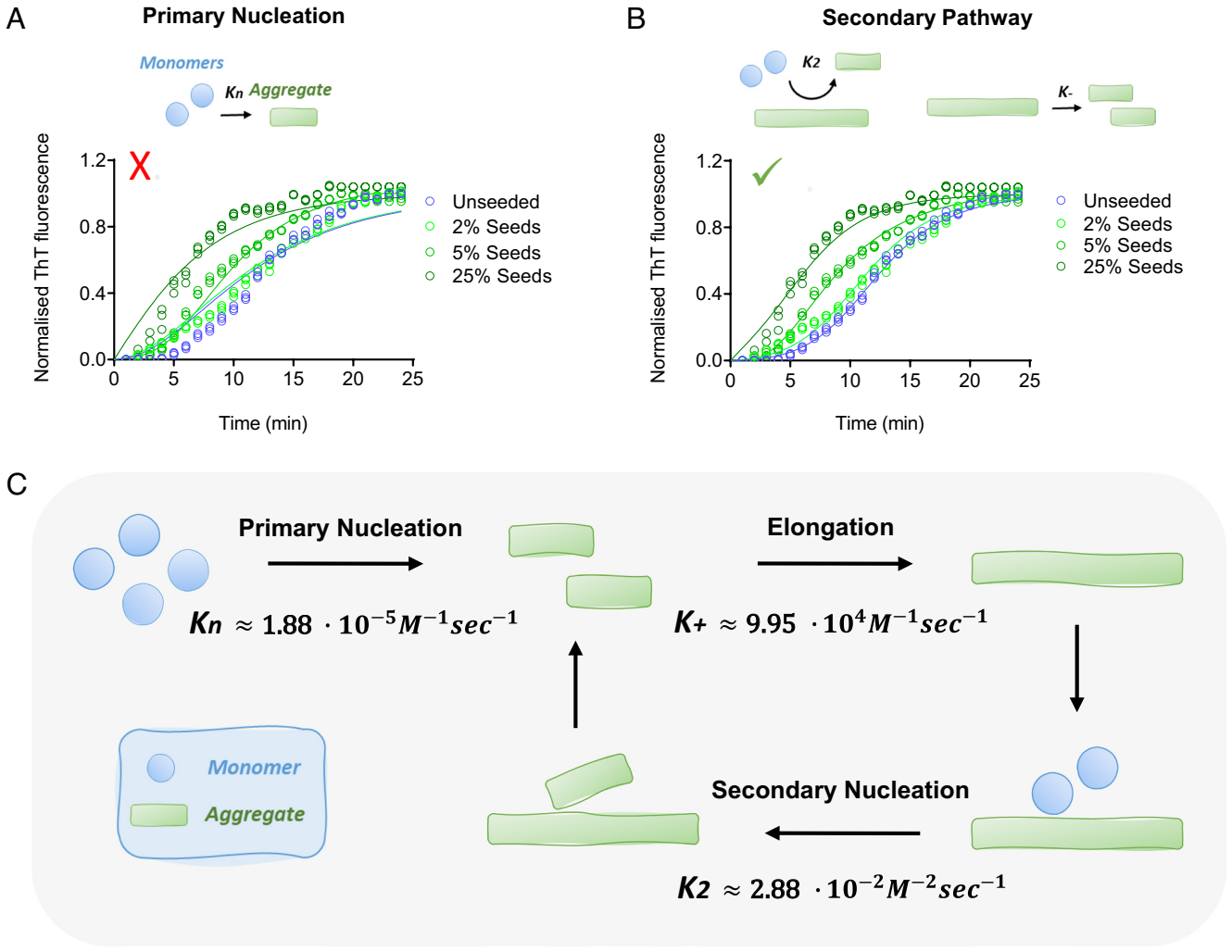


**Fig. 6.** Secondary processes dominate α-synuclein aggregate proliferation within liquid condensates at physiological pH. (*A* and *B*) Analysis of the results of the ThT aggregation assay using AmyloFit, with the normalized aggregation curves measured as a function of time from the unperturbed system (blue), as well as in the presence of 2% (light green), 5% (green) and 25% (dark green) seeds. The graphs represent the best fits of different models in which, respectively, primary nucleation (*A*) and secondary processes (*B*) are assumed to be the dominant mechanism of aggregation. The mean residual errors were 0.009 (with $n_c = 2$) (*A*) and 0.002 with ($n_c = 2, n_2 = 1$) (*B*). The solid lines represent the best fit to each respective condition. We used $m_0 = 30$ mM in all fits. For the unseeded assay we used $M_0 = 0$, and for the seeded assay we used $M_0 = 36.3$, 90.75 and 453.75 μM for 2%, 5% and 25% seeds, respectively. All experiments were performed three times using 75 μM α-synuclein in 50 mM Tris-HCl (pH 7.4) in the presence of 10% PEG and 20 μM ThT. (*C*) Illustration of the microscopic processes involved in α-synuclein aggregation, in the case when fragmentation is not contributing significantly, using the assay reported in this work. The associated rate constants are also reported. Despite the low values of the rate constants for primary nucleation and secondary nucleation, the aggregation process proceeds rapidly within the dense phase because of the high concentration of α-synuclein.

the concentration of α-synuclein in fibrils (referred to as fibril concentration) inside the condensate (*Methods*), where 24.2 is the constant obtained from the slope of the calibration curve, $c^I$ refers to the fibrils partitioned inside the condensate, and $c^{tot}$ refers to the total fibril concentration added to the system (1.5 and 18.75 μM) (Fig. 5*C*). Using Equations 1 to 5 (*Methods*), the concentration of preformed fibrils within condensates at 25% seeds was estimated to be at 454 μM (Fig. 5 *A*–*D*).

Having obtained the concentrations of preformed fibrils within condensates, we tested the fit of the seeded kinetics data to two different models (Fig. 6). The first fit shows that the aggregation data are not well described by a model that includes only primary nucleation and elongation. In contrast, the model with secondary processes resulted in a good fit (Fig. 6). As primary nucleation and secondary nucleation have a different concentration dependence, if we assume that fragmentation does not contribute significantly to aggregate proliferation under the conditions used (no shaking), the critical fibril concentration at which secondary nucleation becomes the dominant mechanism is 20 mM in our system (ratio of the primary to secondary nucleation rate constants (15), $K_n/K_2m_o$, Fig. 6).

## Conclusions

We have determined the microscopic processes governing the aggregation of α-synuclein within liquid condensates (Fig. 6). Our approach has enabled the quantification of the rate constants for α-synuclein spontaneous homogenous primary nucleation and rapid aggregate-dependent aggregate proliferation at physiological pH. We anticipate that this approach will promote further studies to establish whether α-synuclein aggregation via the phase separation pathway is relevant to the onset and progression of Parkinson's disease. In perspective, the possibility of studying the aggregation process of α-synuclein under physiological conditions with the fast and reliable assays that we have reported may open opportunities for screening compounds to inhibit α-synuclein aggregation and its pathological consequences in Parkinson's disease and related synucleinopathies.

## Materials and Methods

The methods of purification and labeling of the proteins are described in *SI Appendix, Materials and Methods*. The methods of monitoring the phase separation and the aggregation of the proteins are also described in *SI Appendix, Materials and Methods*. The details of all experimental assays are reported in *SI Appendix, Materials and Methods*.

**Data, Materials, and Software Availability.** All study data are included in the article and/or supporting information.

**ACKNOWLEDGMENTS.** STD acknowledges funding from the Biotechnology and Biological Sciences Research Council (BBSRC; BB/M011194/1).

Author affiliations: [a]Department of Chemistry, Centre for Misfolding Diseases, University of Cambridge, Cambridge CB2 1EW, UK; [b]Department of Chemistry, Federal University of São Carlos, São Carlos, 13565-905 São Paulo, Brazil; [c]Department of Biology, Institute of Biochemistry, ETH Zurich, 8093 Zurich, Switzerland; and [d]Bringing Materials to Life Initiative, ETH Zurich, 8093 Zurich, Switzerland

1. V. L. Feigin *et al.*, Global, regional, and national burden of neurological disorders, 1990–2016: A systematic analysis for the global burden of disease study 2016. *Lancet Neurol.* **18**, 459–480 (2019).
2. R. Balestrino, A. Schapira, Parkinson disease. *Eur. J. Neurol.* **27**, 27–42 (2020).
3. M. Goedert, M. G. Spillantini, K. Del Tredici, H. Braak, 100 years of Lewy pathology. *Nat. Rev. Neurol.* **9**, 13 (2013).
4. S. H. Shahmoradian *et al.*, Lewy pathology in Parkinson's disease consists of crowded organelles and lipid membranes. *Nat. Neurosci.* **22**, 1099–1109 (2019).
5. M. G. Spillantini *et al.*, α-synuclein in Lewy bodies. *Nature* **388**, 839–840 (1997).
6. J. T. Bendor, T. P. Logan, R. H. Edwards, The function of α-synuclein. *Neuron* **79**, 1044–1066 (2013).
7. H. A. Lashuel, C. R. Overk, A. Oueslati, E. Masliah, The many faces of α-synuclein: From structure and toxicity to therapeutic target. *Nat. Rev. Neurosci.* **14**, 38–48 (2013).
8. M. H. Polymeropoulos *et al.*, Mutation in the α-synuclein gene identified in families with Parkinson's disease. *Science* **276**, 2045–2047 (1997).
9. A. Singleton *et al.*, Alpha-synuclein locus triplication causes Parkinson's disease. *Science* **302**, 841–842 (2003).
10. S. I. Cohen, M. Vendruscolo, C. M. Dobson, T. P. Knowles, From macroscopic measurements to microscopic mechanisms of protein aggregation. *J. Mol. Biol.* **421**, 160–171 (2012).
11. T. P. Knowles, M. Vendruscolo, C. M. Dobson, The amyloid state and its association with protein misfolding diseases. *Nat. Rev. Mol. Cell Biol.* **15**, 384–396 (2014).
12. A. K. Buell *et al.*, Solution conditions determine the relative importance of nucleation and growth processes in α-synuclein aggregation. *Proc. Natl. Acad. Sci. U.S.A.* **111**, 7671–7676 (2014).
13. C. Galvagnion *et al.*, Lipid vesicles trigger α-synuclein aggregation by stimulating primary nucleation. *Nat. Chem. Biol.* **11**, 229–234 (2015).
14. T. C. Michaels *et al.*, Dynamics of oligomer populations formed during the aggregation of Alzheimer's Aβ42 peptide. *Nat. Chem.* **12**, 445–451 (2020).
15. S. I. Cohen *et al.*, Proliferation of amyloid-β42 aggregates occurs through a secondary nucleation mechanism. *Proc. Natl. Acad. Sci. U.S.A.* **110**, 9758–9763 (2013).
16. R. Gaspar *et al.*, Secondary nucleation of monomers on fibril surface dominates α-synuclein aggregation and provides autocatalytic amyloid amplification. *Q. Rev. Biophys.* **50**, e6 (2017).
17. C. Galvagnion *et al.*, Chemical properties of lipids strongly affect the kinetics of the membrane-induced aggregation of α-synuclein. *Proc. Natl. Acad. Sci. U.S.A.* **113**, 7065–7070 (2016).
18. S. Ray *et al.*, α-synuclein aggregation nucleates through liquid–liquid phase separation. *Nat. Chem.* **12**, 705–716 (2020).
19. M. C. Hardenberg *et al.*, Observation of an α-synuclein liquid droplet state and its maturation into Lewy body-like assemblies. *J. Mol. Cell Biol.* **13**, 282–294 (2021).
20. M. Hardenberg, A. Horvath, V. Ambrus, M. Fuxreiter, M. Vendruscolo, Widespread occurrence of the droplet state of proteins in the human proteome. *Proc. Natl. Acad. Sci. U.S.A.* **117**, 33254–33262 (2020).
21. E. G. Stender *et al.*, Capillary flow experiments for thermodynamic and kinetic characterization of protein liquid-liquid phase separation. *Nat. Comm.* **12**, 1–18 (2021).
22. S. F. Banani, H. O. Lee, A. A. Hyman, M. K. Rosen, Biomolecular condensates: Organizers of cellular biochemistry. *Nat. Rev. Mol. Cell Biol.* **18**, 285–298 (2017).
23. Y. Shin, C. P. Brangwynne, Liquid phase condensation in cell physiology and disease. *Science* **357**, eaaf4382 (2017).
24. M. Fuxreiter, M. Vendruscolo, Generic nature of the condensed states of proteins. *Nat. Cell Biol.* **117**, 587–594 (2021).
25. A. S. Lyon, W. B. Peeples, M. K. Rosen, A framework for understanding the functions of biomolecular condensates across scales. *Nat. Rev. Mol. Cell Biol.* **22**, 1–21 (2020).
26. S. Alberti, A. A. Hyman, Biomolecular condensates at the nexus of cellular stress, protein aggregation disease and ageing. *Nat. Rev. Mol. Cell Biol.* **22**, 196–213 (2021).
27. C. Mathieu, R. V. Pappu, J. P. Taylor, Beyond aggregation: Pathological phase transitions in neurodegenerative disease. *Science* **370**, 56–60 (2020).
28. A. L. Darling, J. Shorter, Combating deleterious phase transitions in neurodegenerative disease. *Biochim. Biophys. Acta Mol. Cell Res.* **1868**, 118984 (2021).
29. M. Vendruscolo, M. Fuxreiter, Protein condensation diseases: Therapeutic opportunities. *Nat. Comm.* **13**, 1–11 (2022).
30. S. Ambadipudi, J. Biernat, D. Riedel, E. Mandelkow, M. Zweckstetter, Liquid–liquid phase separation of the microtubule-binding repeats of the Alzheimer-related protein tau. *Nat. Comm.* **8**, 1–13 (2017).
31. W. M. Babinchak *et al.*, The role of liquid–liquid phase separation in aggregation of the TDP-43 low-complexity domain. *J. Biol. Chem.* **294**, 6306–6317 (2019).
32. A. Patel *et al.*, A liquid-to-solid phase transition of the ALS protein FUS accelerated by disease mutation. *Cell* **162**, 1066–1077 (2015).
33. S. Wegmann *et al.*, Tau protein liquid–liquid phase separation can initiate tau aggregation. *EMBO J.* **37**, e98049 (2018).
34. A. Molliex *et al.*, Phase separation by low complexity domains promotes stress granule assembly and drives pathological fibrillization. *Cell* **163**, 123–133 (2015).
35. C. Yuan *et al.*, Nucleation and growth of amino acid and peptide supramolecular polymers through liquid–liquid phase separation. *Angew. Chem.* **131**, 18284–18291 (2019).
36. N. M. Kanaan, C. Hamel, T. Grabinski, B. Combs, Liquid-liquid phase separation induces pathogenic tau conformations in vitro. *Nat. Comm.* **11**, 1–16 (2020).
37. T. P. Knowles *et al.*, An analytical solution to the kinetics of breakable filament assembly. *Science* **326**, 1533–1537 (2009).
38. A. Levin *et al.*, Ostwald's rule of stages governs structural transitions and morphology of dipeptide supramolecular polymers. *Nat. Comm.* **5**, 1–8 (2014).
39. G. Meisl *et al.*, Molecular mechanisms of protein aggregation from global fitting of kinetic models. *Nat. Protoc.* **11**, 252–272 (2016).
40. A. Dong, P. Huang, W. S. Caughey, Protein secondary structures in water from second-derivative amide i infrared spectra. *Biochemistry* **29**, 3303–3308 (1990).
41. W. K. Surewicz, H. H. Mantsch, New insight into protein secondary structure from resolution-enhanced infrared spectra. *Biochim. Biophys. Acta* **952**, 115–130 (1988).
42. F. S. Ruggeri *et al.*, Infrared nanospectroscopy reveals the molecular interaction fingerprint of an aggregation inhibitor with single Aβ42 oligomers. *Nat. Comm.* **12**, 1–9 (2021).
43. S. Boyko, X. Qi, T.-H. Chen, K. Surewicz, W. K. Surewicz, Liquid–liquid phase separation of tau protein: The crucial role of electrostatic interactions. *J. Biol. Chem.* **294**, 11054–11059 (2019).
44. G. Krainer *et al.*, Reentrant liquid condensate phase of proteins is stabilized by hydrophobic and non-ionic interactions. *Nat. Comm.* **12**, 1–14 (2021).
45. S. Kroschwald, S. Maharana, A. Simon, Hexanediol: A chemical probe to investigate the material properties of membrane-less compartments. *Matters* **3**, e201702000010 (2017).
46. J. A. Riback, C. P. Brangwynne, Can phase separation buffer cellular noise? *Science* **367**, 364–365 (2020).
47. A. Klosin *et al.*, Phase separation provides a mechanism to reduce noise in cells. *Science* **367**, 464–468 (2020).

# Supplementary Information

***Purification and labelling of α-synuclein***

Human wild-type α-synuclein and its cysteine variant A90C were expressed and purified as previously described, using *E. coli* BL21 (DE3)-gold competent cells (Agilent Technologies) transformed with the pT7-7 plasmid encoding α-synuclein. Expression was induced by the addition of 1 mM isopropyl β-d-1-thiogalactopyranoside (IPTG) (1). Following purification, the proteins were concentrated, and buffer exchanged into either 50 mM trisaminomethane-hydrochloride (Tris-HCl), 20 mM sodium phosphate (NaPi) or phosphate buffered saline (PBS) at pH 7.4 using Amicon Ultra-15 Centrifugal Filter Units (Merck Millipore). The A90C variant was labelled with 1.5-fold molar excess of C5 maleimide-linked Alexa Fluor 647 (Invitrogen Life Technologies) overnight at 4 °C under constant gentle stirring. The unbound dye was removed using Amicon Ultra-15 Centrifugal Filter Units and buffer exchanged into either 50 mM Tris-HCl, 20 mM NaPi or PBS at pH 7.4. The final protein concentration was measured using ultraviolet-visible (UV-vis) spectroscopy on a Cary 100 system (Agilent Technologies). All proteins were aliquoted, flash-frozen in liquid nitrogen, stored at -80 °C and thawed once before each experiment.

***Preparation and labelling of preformed α-synuclein fibrils***

Preformed α-synuclein fibrils were formed from recombinant α-synuclein wild-type or cysteine variant (A90C) monomers diluted in buffer (50 mM Tris-HCl at pH 7.4) to concentrations of approximately 500 μM. Monomers in microcentrifuge Eppendorf tubes (Axygen low-bind tubes) were incubated at 40 °C, with constant stirring speed (1,500 rpm) with a teflon bar and left to fibrillate on an RCT Basic Heat Plate (RCT Basic, model no. 0003810002; IKA, Staufen, Germany) for up to 72 h. Samples were centrifuged (Centrifuge 5427 R) at 4 °C, 14,000 rpm for 15 min. The supernatant was used to determine the monomer concentration and fibril concentration was determined as monomer equivalents. For visualisation purposes, A90C α-synuclein fibrils were labelled with 1.5-fold molar excess of C5 maleimide-linked Alexa Fluor 488 (Invitrogen Life Technologies) overnight at 4 °C under constant but gentle stirring. The excess dye was removed by at least 3 sequential 50 mM Tris-HCl washes by centrifugation (4 °C, pH 7.4, 14,000 rpm) for 15 min. Before each experiment, seed fibrils were pre-treated by 15 sec (15 pulses) sonication at 10% power with 50% duty cycle using a Microtip sonicator (Bandelin Sonopuls HD2070) to disperse lumped fibrils.

***α-Synuclein phase separation assay***

Non-labelled wild-type α-synuclein was mixed with the A90C variant labelled with Alexa Fluor 647 at a 100:1 molar ratio in either 50 mM Tris-HCl, 20 mM NaPi or PBS (pH 7.4) and 10% polyethylene

glycol 10,000 (PEG) (Thermo Fisher Scientific) or labelled maleimide PEG FITC (Fluorescein) 10,000 (NANOCS) by volume at room temperature (20-22 °C). Additionally, NaCl, 1,6-hexanediol and dimethyl sulfoxide (DMSO) and preformed fibrils were supplemented in the phase separation assay. 10 µL of the final mixture was pipetted on a 35 mm glass bottom dish (P35G-1.5-20-C, MatTek Life Sciences) and immediately imaged on a Leica TCS SP8 inverted confocal microscope using a 60×/1.4 HC PL Apo CS oil objective (Leica Microsystems). The excitation wavelength was set to 633 nm for all experiments. All images were processed and analysed in ImageJ (NIH).

***Fluorescence spectra***

The excitation and emission spectra of 20 mM solutions of thioflavin T (ThT), Alexa Fluor 488 and Alexa Fluor 647 were obtained on a Cary Eclipse fluorescence spectrometer (Agilent). The emission and excitation wavelength used were $\lambda_{ex}$=440 nm/$\lambda_{em}$=480 nm for ThT, $\lambda_{ex}$=496 nm/$\lambda_{em}$=520 nm for Alexa488 and $\lambda_{ex}$=650 nm/$\lambda_{em}$=665 nm for Alexa647. The spectra were plotted using Graphpad Prism.

***Preformed fibril bound thioflavin T (ThT) assay***

To study the concentration-dependent emission of fibril-bound ThT, wild-type α-synuclein preformed fibrils (100, 75, 50, 20 and 10 µM) were incubated with 20 µM ThT in 50 mM Tris-HCl and 10% PEG. For control monomeric wild-type α-synuclein were also treated with 20 µM ThT in 50 mM Tris-HCl and 10% PEG. 10 µL of the final mixture was pipetted on a 35 mm glass bottom dish and immediately imaged on a Leica TCS SP8 inverted confocal microscope using a 60×/1.4 HC PL Apo CS oil objective (Leica Microsystems). The excitation wavelength was 488 nm for all ThT-based experiments. All images were processed and analysed in ImageJ (NIH).

***Fluorescence recovery after photobleaching (FRAP) experiment***

FRAP experiments were performed on condensates using a Leica Stellaris Will inverted stage scanning confocal microscope. To conduct FRAP experiments, a 63x magnification oil objective (63x/1.4 HC PL Apo CS oil) was used. Bleaching was done using the 647 nM laser at 20% intensity for 2 sec following a 2 sec pre-beach sequence. Immediate post-beach images were captured at 500 ms per frame rate for 55 sec. Intensity traces of bleached area were background corrected and normalised to reference signal and FRAP time which is defined by the time to half maximal signal recovery. This was determined using the FRAP wizard system (Leica) on the confocal microscope.

***Transmission electron microscopy (TEM)***

α-Synuclein samples from the ThT-based aggregation assay were obtained prior to fibril formation mediated by phase separation and after fibril formation. The obtained sample (5 µL) was deposited on a carbon film of 400 mesh 3 mm copper grid. The grids were washed once with Milli-Q water, then

incubated with 1% (w/v) uranyl acetate for 2 min and washed twice again with Milli-Q water before being air-dried at room temperature. Samples were imaged at the Cambridge Advanced Imaging Centre using a Tecnai G2 transmission electron microscope operating at 80–200 keV.

***Circular dichroism (CD)***

Protein samples spectra containing non-labelled wild-type α-synuclein was mixed with the A90C variant labelled with Alexa Fluor 647 at a 100:1 molar ratio in 50 mM Tris-HCl, (pH 7.4), 10% polyethylene glycol 10,000 (PEG) were diluted 1:10 in 50mM TRIS (pH 7.4) and 20 μM ThT. were obtained on a JASCXO J-810 (Easton, USA) using quartz cuvettes with path lengths of 1mm by averaging 8 separate spectra each recorded between 200nm-250nm, with 1nm bandwidth, 0.5nm data pitch, scanning speed of 50nm/min and a 1s response time.

***Fourier-transform infrared spectroscopy (FTIR)***

Product from phase separation assay prior to condensate formation and upon amyloid formation were washed off glass slide with 50 mM Tris-HCL, 50 μM monomeric α-synuclein were seeded with 1 μL of product formed through phase separation at unknown concentration. Reaction mixture left in a plate reader for 24 h to aggregate quiescently. Once ThT fluorescence reached saturated, reactions were stopped, and products were recovered from microplate wells. Product was centrifuged at 12,000 rpm for 10 min, at 4 °C. Supernatant containing soluble α-synuclein was discarded, and pellets were washed twice with $H_2O$. Pellets were resuspended in 3 μL $H_2O$ and subjected to attenuated total reflectance (ATR) Fourier transform infrared (FTIR) spectroscopy. 1.5 μL of solute was applied to a Perkin-Elmer Spectrum100 FTIR with an ATR diamond attachment and dried using dry air. Prior to scanning, sample and electronics chambers were purged with a constant flow of dry air. 100 replicate scans were averaged from 4000 to 800 $cm^{-1}$, normalized to amide I intensity (~ 1630 $cm^{-1}$ peak), and second derivatives were taken with 9 points for slope analysis.

***α-Synuclein aggregation assay within dense liquid condensates***

20 or 40 μM ThT (Sigma) and additional compounds and preformed fibrils, depending on the experiments, were mixed with monomeric wild-type α-synuclein, containing 1 molar % A90C α-synuclein labelled with Alexa Fluor 647 prior to each experiment. The assay mixture, which included 50 mM Tris-HCl, pH 7.4, 10% PEG 10,000, was pipetted onto a 35 mm glass bottom dish and imaged on a Leica TCS SP8 inverted confocal microscope using a 60×/1.4 HC PL Apo CS oil objective. The excitation wavelength 633 nm and 488 nm were used for Alexa Fluor 647 labelled α-synuclein and ThT, respectively. Images were processed in ImageJ; an area adjacent to the edge of the droplet was cropped and analysed, thus allowing for time-dependent measurement of amyloid formation.

***Estimation of the α-synuclein concentration required for phase separation in water-in-oil droplets***

*Fabrication of microfluidic devices*. The fabrication process of the microfluidics was taken from a previously established protocol (2-4). In brief, a soft photolithographic process was used to fabricate the master through which microfluidic devices were made. A 50 μm photoresist (SU-8 3050, MicroChem) was spin-coated onto a silicon wafer. This was soft baked at 95 °C for 3 min. A film mask was placed on the wafer and the whole system was exposed in UV light to induce polymerization. The wafer was then baked at 95 °C for 30 min. Finally, the master was placed into a solution of propylene glycol methyl ether acetate (PGMEA, Sigma-Aldrich), which helped in the development process. Elastomer polydimethylsiloxane (PDMS) with curing agent (Sylgard 184, DowCorning, Midland, MI) was mixed at a ratio of 10:1 to fabricate the devices. This mixture was then incubated at 65 °C and cured for a total of 3 h. Once hardened, the PDMS was peeled off the master, and holes were punched into the PDMS, which acted as inlets and outlets. Finally, the PDMS slab was bound to a glass slide by treatment with a plasma bonder (Diener Electronic, Ebhausen, Germany).

*Formation and confinement of droplets. neMESYS syringe pumps*. Syringe pumps (Cetoni, Korbussen, Germany) were used to control the flow rates within the microchannels. Protein solution was mixed with PEG at a ratio of 1:1 at the first junction. At the second junction, the oil phase, which consisted of fluorinated oil (Fluorinert FC-40, Sigma-Aldrich) and 2% w/w fluorosurfactant (RAN biotechnologies) intersected the aqueous phase resulting in water-in-oil droplets being formed. Following droplet generation, droplets were confined within a microfluidic trap (3, 4). In brief, droplets are directed towards an array of traps whereby once a droplet is driven within the microfluidic confinement, it is unable to escape unless a pressure is applied from the outlet. Droplets were then incubated at room temperature to allow for shrinkage. This resulted in an increase of the local concentration of protein and PEG within the droplets which led to protein phase separation. The water-in-oil droplets and the protein phase separation was monitored using fluorescence microscopy.

*Calculation of protein concentration during phase separation*. The concentration of the protein was obtained by calculating the ratio of the droplet volume just after trapping ($V_1$) and at the point of phase separation ($V_2$), i.e. at the point at which condensates start appearing within the water-in-oil droplet. By multiplying the initial monomeric protein concertation by the value of this ratio, the actual protein concentration at the point of phase separation could be determined.

***Estimation of α-synuclein concentration in condensates***

The fluorescence calibration was performed by imaging solutions of the Alexa Fluor 647 dye at 1000, 500, 200, 100, 50, 20 and 1 mM in 50 mM Tris-HCl at pH 7.4 with the addition of 10% PEG. Using the same acquisition settings, images were taken of α-synuclein condensates at 400, 100, 75, 50 and 25 μM 10 min after phase separation to estimate the local concentration of α-synuclein in condensates.

Several condensates (approximately 70 per concentration) were analysed by drawing a circular region of interest around the condensate to obtain the average pixel intensity. Linear regression analysis of the intensity of Alexa Fluor 647 calibration images ($r^2$ = 0.92) was used to interpolate the estimated concentration of α-synuclein proteins within condensates.

***Estimation of the concentration of preformed α-synuclein fibrils in condensates***

A calibration of the Alexa Fluor 488 fluorescence intensity was carried out using various fibril concentrations of A90C α-synuclein labelled with Alexa Fluor 488 in 50 mM Tris-HCl at pH 7.4 with the addition of 10% PEG. Using the same acquisition settings, images were taken of α-synuclein condensates 6 min after phase separation at 75 μM containing 2% and 25% Alexa Fluor 488 labelled preformed fibrils to estimate the local concentration of preformed fibrils within the liquid droplet. Several condensates (approximately 100) were analysed by drawing a circular region of interest around the condensate to obtain the average pixel intensity for each droplet. Linear regression analysis of the intensity of Alexa Fluor 488 fibrils images ($r^2$ = 0.82) was used to estimate the concentration of α-synuclein preformed fibrils within condensates (**Figure 4C**).

If we consider a system of total volume $V$ and containing a dense phase coexisting with a dilute phase, the dense phase (which we term phase I) occupies a volume $V^I$, while the volume of the dilute phase (which we term phase II) is $V^{II} = V - V^I$, such that

$$V = V^I + V^{II} \quad (1)$$

If we add to this system a total concentration $c^{tot}$ of preformed fibrils, these fibrils will partition differently in phases I and II depending on their relative interaction with the dense and dilute phases. We capture this behaviour by means of the partitioning coefficient Γ, defined as

$$\Gamma = \frac{c^I}{c^{II}} \quad (2)$$

While Γ can be determined from the Flory-Huggins theory of phase separation (5), we will consider it as a known parameter in our calculations, where $c^I$ and $c^{II}$ are the concentrations of preformed fibrils in phases I and II, respectively. The total fibril concentration in the system is the average of the concentrations $c^I$ and $c^{II}$ weighted by the volumes of the respective phases

$$c^{tot} = \frac{V^I}{V} c^I + \frac{V^{II}}{V} c^{II} \quad (3)$$

This condition states that the total number of fibrils in the system is conserved. By combining Eqs. (1), (2) and (3) we can solve for $c^I$ and $c^{II}$ and find

$$c^I = \xi\, \Gamma\, c^{tot}, \qquad c^{II} = \xi\, c^{tot} \tag{4a}$$

where

$$\xi = \frac{1}{1+(\Gamma-1)\, V^I/V} \tag{4b}$$

Using Eq. (4) we can calculate the concentration of fibrils in the condensed phase from $c^{tot}$, Γ and $V^I/V$. In the limit when $\Gamma \to \infty$ (when the fibrils partition mostly inside the condensed phase), Eq. (4) reduces to

$$c^I = \frac{V}{V^I} c^{tot}, \qquad c^{II} = 0 \qquad (5)$$

In this regime, we have a linear relationship linking $c^I$ to $c^{tot}$. The slope of this relationship is $V/V^I$ and relates to the volume fraction $V^I/V$ occupied by the dense phase. In our experiments we measured $c^I = 36.6$ μM for $c^{tot} = 1.5$ μM and $c^I = 453.75$ μM for $c^{tot} = 18.75$ μM. With these data points we estimated a slope $V/V^I = 24.2$.

***Image analysis of α-synuclein condensates***

Images of wild-type α-synuclein, containing 1 molar % α-synuclein Alexa Fluor 647 labelled A90C α-synuclein were acquired on a Leica TCS SP8 inverted confocal microscope system. All images within an experiment were acquired using identical confocal settings (scan speed, resolution, magnification, laser intensity, gain, and offset). Images were analysed by applying threshold functions in ImageJ software that identified the phase separated α-synuclein condensates and excluded the background of the image. All condensates within the threshold limits were analysed for total area (μm$^2$), average size of individual droplets (μm$^2$) and mean fluorescence intensity of individual condensates (arbitrary units) (**Figure S6**).

***AmyloFit data analysis***

The experimental ThT fluorescence readout was uploaded on the free online platform AmyloFit(6) (https://www.amylofit.ch.cam.ac.uk). The software normalised the data to 0% and 100% by averaging the values at the baseline and the plateau of the reaction. Upon data normalisation, the concentration of aggregate mass could be observed as a function of time. A basin-hopping algorithm was applied to fit the experimental data to a model of protein aggregation. The initial monomer concentration ($m_0$) was

set to 30 mM. Reaction orders for primary and secondary nucleation were set to 2. The number of basin hops was set to 40 for each fit. The AmyloFit user manual can be consulted for more in-depth information on the fitting procedure (6). We note that at the high concentrations of α-synuclein in the condensates, correction terms for the activity coefficients may be added to the equations. This is currently under consideration.

***Statistical analysis***

All statistical analyses were performed in GraphPad Prism 8 (GraphPad Software). Data are presented as means ± SEM from at least 3 independent biological replicates, unless indicated otherwise. The statistical significance was analysed either by 2-tailed Student's t test or one-way ANOVA followed by Bonferroni's multiple-comparison.

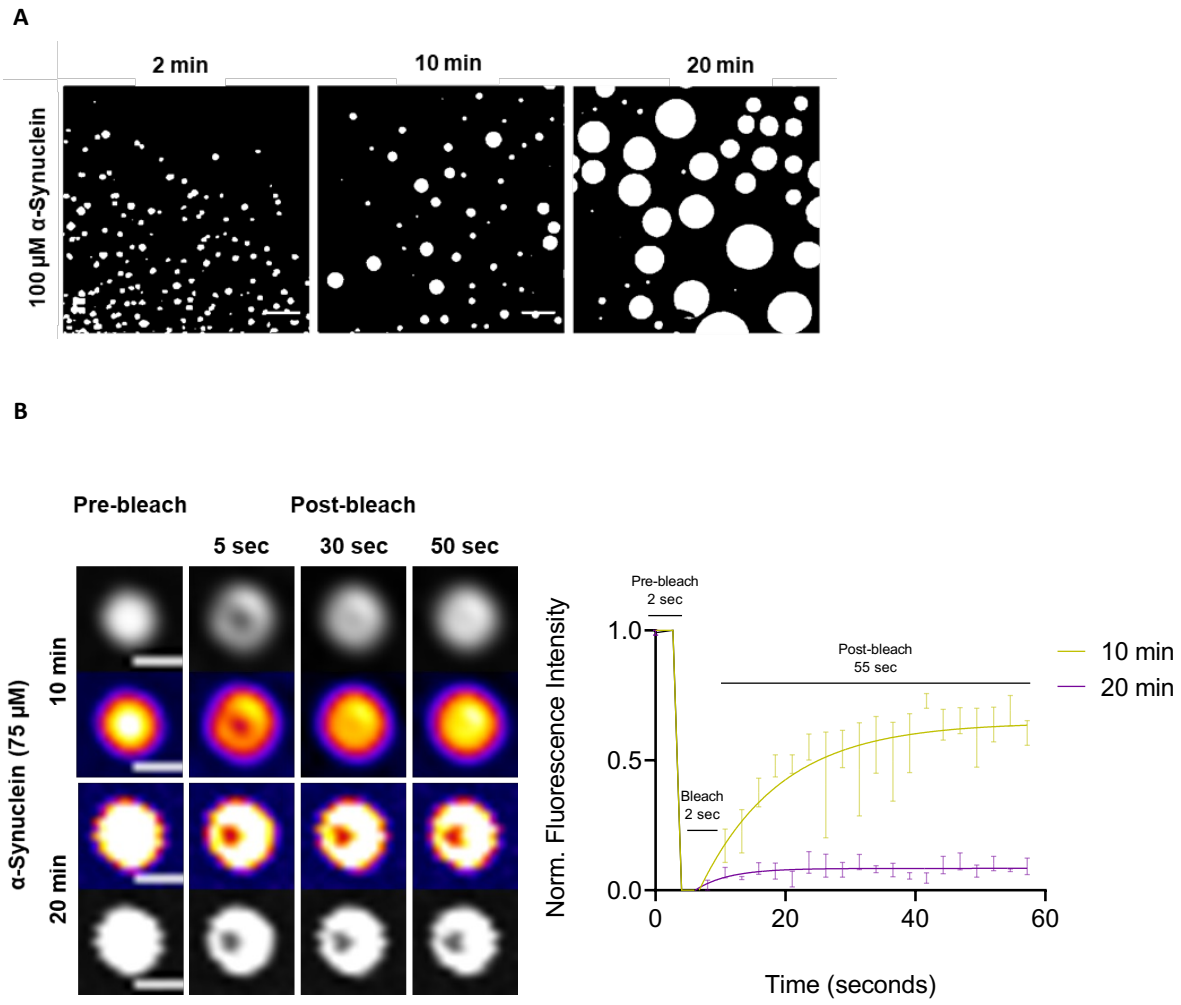


**Supplementary Figure 1. α-Synuclein condensates undergo a transition from liquid-like to solid-like forms over time.** (**A**) Fluorescence microscopy images displaying formation of α-synuclein condensates (75 µM) at 2, 10 and 20 min. The scale bar indicates 10 µm. (**B**) FRAP measurements of 75 µM α-synuclein condensates at 10 and 20 min quantify the change in dynamics of condensates over time. The images correspond to the region of interest with pre-bleach and post-bleach condensates at 5, 30 and 50 sec for each condition. The scale bar indicates 2 µm. The data represent the mean ± SEM of n=4 individual experiments.

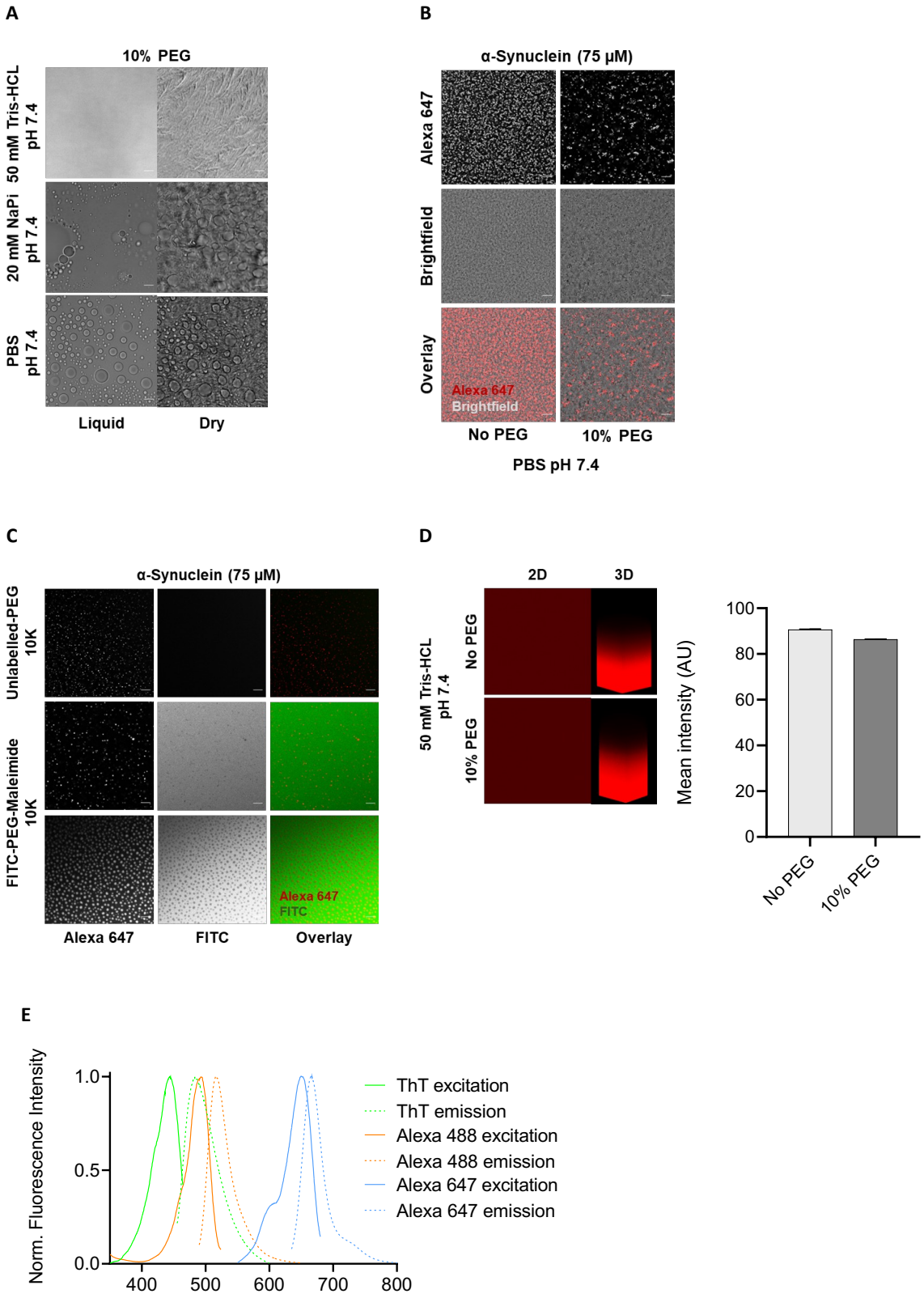


**Supplementary Figure 2. Analysis of the use of 10% PEG to study α-synuclein phase separation under various buffer conditions. (A)** Bright-field images showing the formation of PEG condensates under various buffer conditions at pH 7.4 in the absence of α-synuclein and with 10% PEG: 50 mM Tris-HCl, 20 mM NaPi, and PBS. PEG condensates were observed when 10% PEG and 20 mM NaPi

or PBS were combined. No PEG condensates were observed when 10% PEG and 50 mm Tris-HCl were used. (**B)** Fluorescence microscopy images showing the observed condensate formation of 75 μM α-synuclein (labelled with Alexa Fluor 647) in PBS in the presence and absence 10% PEG. **(C)** Microscopy images of 75 μM α-synuclein (labelled with Alexa Fluor 647) in 50 mM Tris-HCl with the presence of 10K-unlabelled PEG (10%) and 10K FITC (fluorescein isothiocyanate) labelled-PEG-maleimide (10%). **(D)** Alexa Fluor 647 fluorescence intensity in 50 mM Tris-HCl in the presence and absence of 10% PEG. **(E)** Excitation and emission spectra of ThT, Alexa Fluor 488 and Alexa Fluor 647 in the presence of 50 mM Tris-HCl.

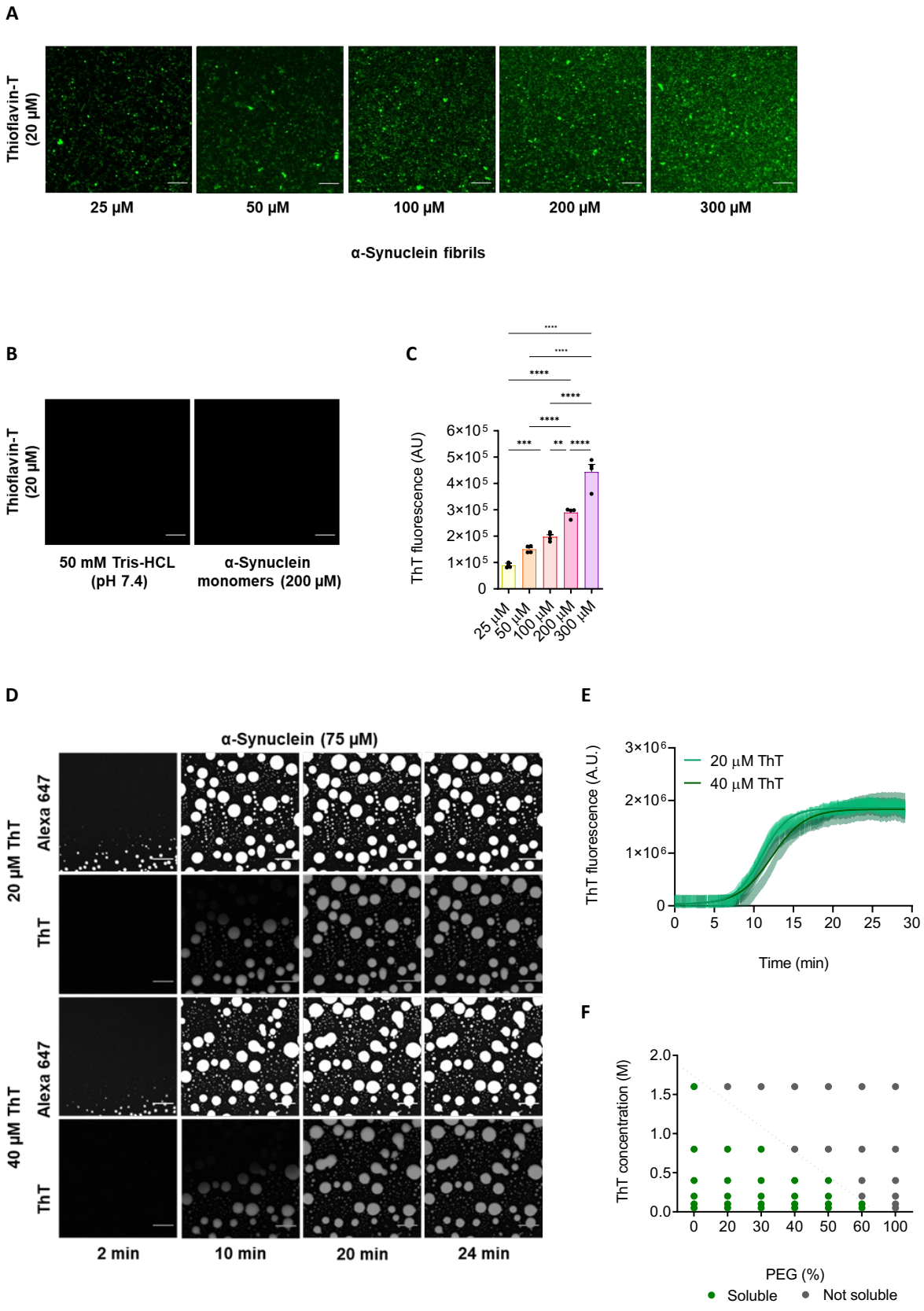


**Supplementary Figure 3. Analysis of the use of ThT as a reporter fluorescent dye for α-synuclein fibril formation within liquid-like condensates. (A)** Fluorescence microscopy images highlighting the concentration dependence of the ThT fluorescence intensity on the amyloid fibril load with

increasing concentration of α-synuclein preformed fibrils (25, 50, 100, 200 and 300 μM) with 20 μM ThT in 50 mM Tris-HCl at pH 7.4. The scale bar represents 10 μm. **(B)** In the absence of amyloid fibrils, ThT fluorescence is not observed. Monomeric α-synuclein (200 μM) and 50 mM Tris-HCl at pH 7.4 in the presence of 20 μM ThT was used for control experiments. **(C)** Quantification of the ThT (20 μM) fibril-dependent fluorescence intensity of the representative images shown in panel A for 25 μM (yellow), 50 μM (orange), 100 μM (red), 200 μM (magenta) and 300 μM (purple) α-synuclein preformed fibrils. All experiments were performed in 50 mM Tris-HCl (pH 7.4) in the presence of 20 μM ThT. **(D)** Fluorescence imaging of α-synuclein condensate and amyloid formation using 20 and 40 μM ThT. The images represent an area of the sample that was tracked over time, showing no detectable changes after 10 min. **(E)** Quantification of 75 μM α-synuclein ThT fluorescence over time of the images shown in panel D for 20 (light green) and 40 (dark green) μM ThT. ThT was measure every 2 sec over 30 min. **(F)** Phase diagram showing the solubility of ThT (powder) at different concentrations for different PEG concentrations. Grey dots indicate ThT insolubility, and green dots indicate ThT solubility. A dotted black line is used for guidance**.** The data represent the mean ± SEM of n=4 individual experiments. One-way ANOVA., **P < 0.01, ***P < 0.001, ****P < 0.0001.

A

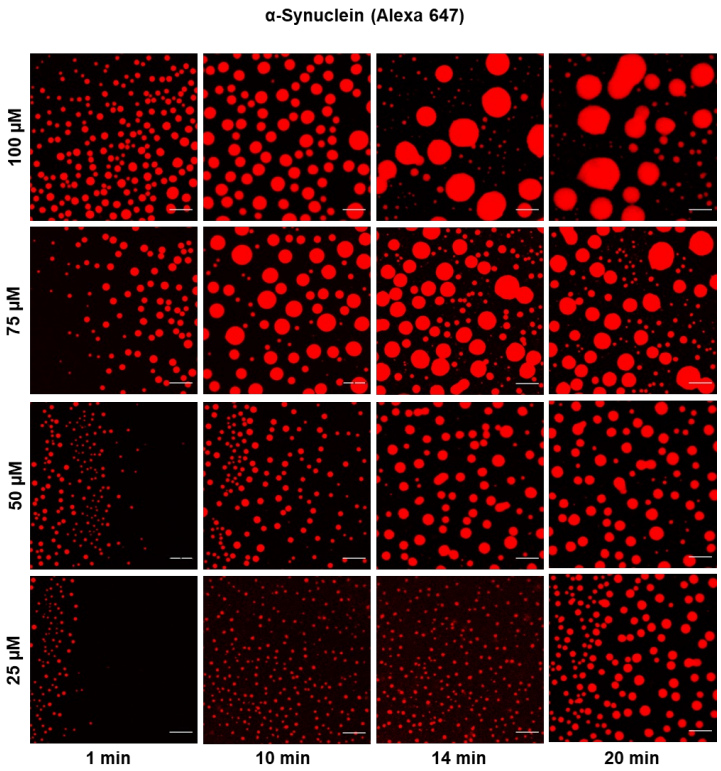
α-Synuclein (Alexa 647)
100 µM
75 µM
50 µM
25 µM
1 min
10 min
14 min
20 min

B

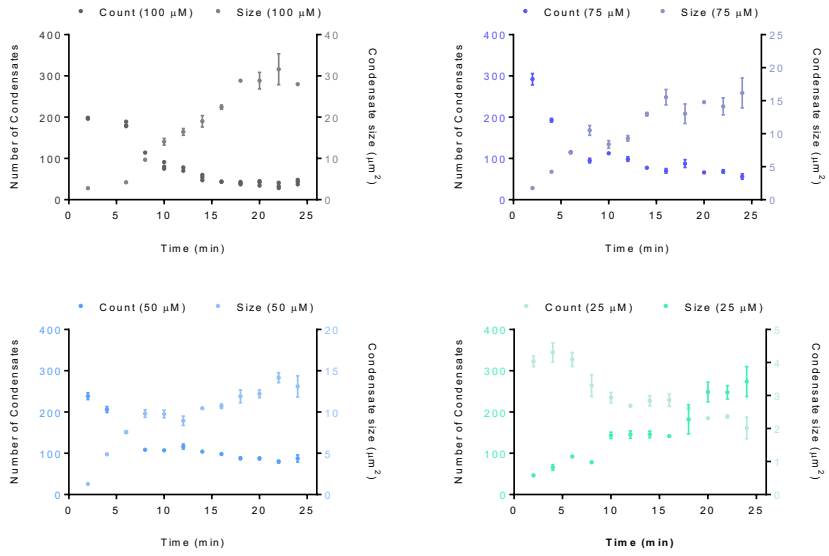
Count (100 µM)
Size (100 µM)
Count (75 µM)
Size (75 µM)
Count (50 µM)
Size (50 µM)
Count (25 µM)
Size (25 µM)
Number of Condensates
Condensate size (µm²)
Time (min)

C

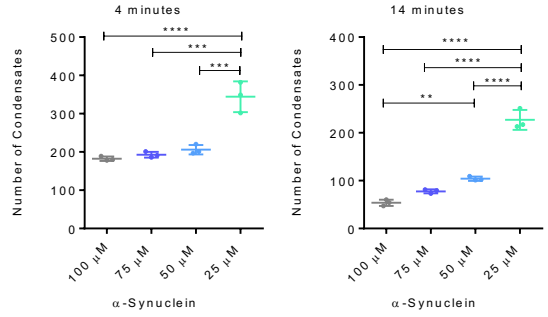
4 minutes
14 minutes
Number of Condensates
100 µM
75 µM
50 µM
25 µM
α-Synuclein

D

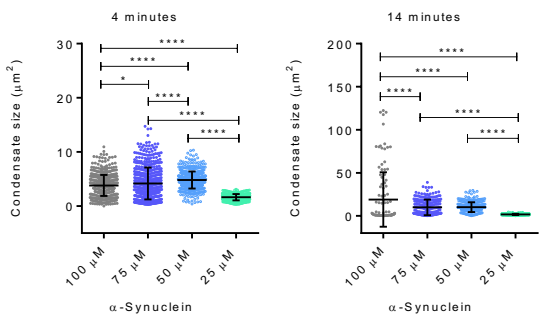
4 minutes
14 minutes
Condensate size (µm²)
100 µM
75 µM
50 µM
25 µM
α-Synuclein

**Supplementary Figure 4. α-Synuclein forms liquid condensates at physiological concentrations under crowding conditions. (A)** Fluorescence microscopy images of α-synuclein forming μm-sized condensates (labelled with Alexa Fluor 647) in the presence of crowding agent (10% PEG) in 50 mM Tris-HCl at physiological concentrations (25 - 100 μM) and pH (7.4) over time. The scale bar represents 10 μm. **(B)** Quantification of condensates number and average size at indicated time points at physiological concentrations of 100 (grey), 75 (blue), 50 (cyan) and 25 (turquoise) μM of α-synuclein under crowded conditions in 50 mM Tris-HCl and pH 7.4. The inverse relation between number (dark colour) and size (light colour) illustrates the growth of the condensates over time. **(C,D)** Quantification of total number (C) and size distribution (D) of condensates at 4 and 14 min after phase separation**.** All experiments were performed in 50 mM Tris-HCl at pH 7.4 in the presence of 10% PEG. The data represent the mean ± SEM of n=3 individual experiments. One-way ANOVA. *P < 0.05, **P < 0.01, ***P < 0.001, ****P < 0.0001.

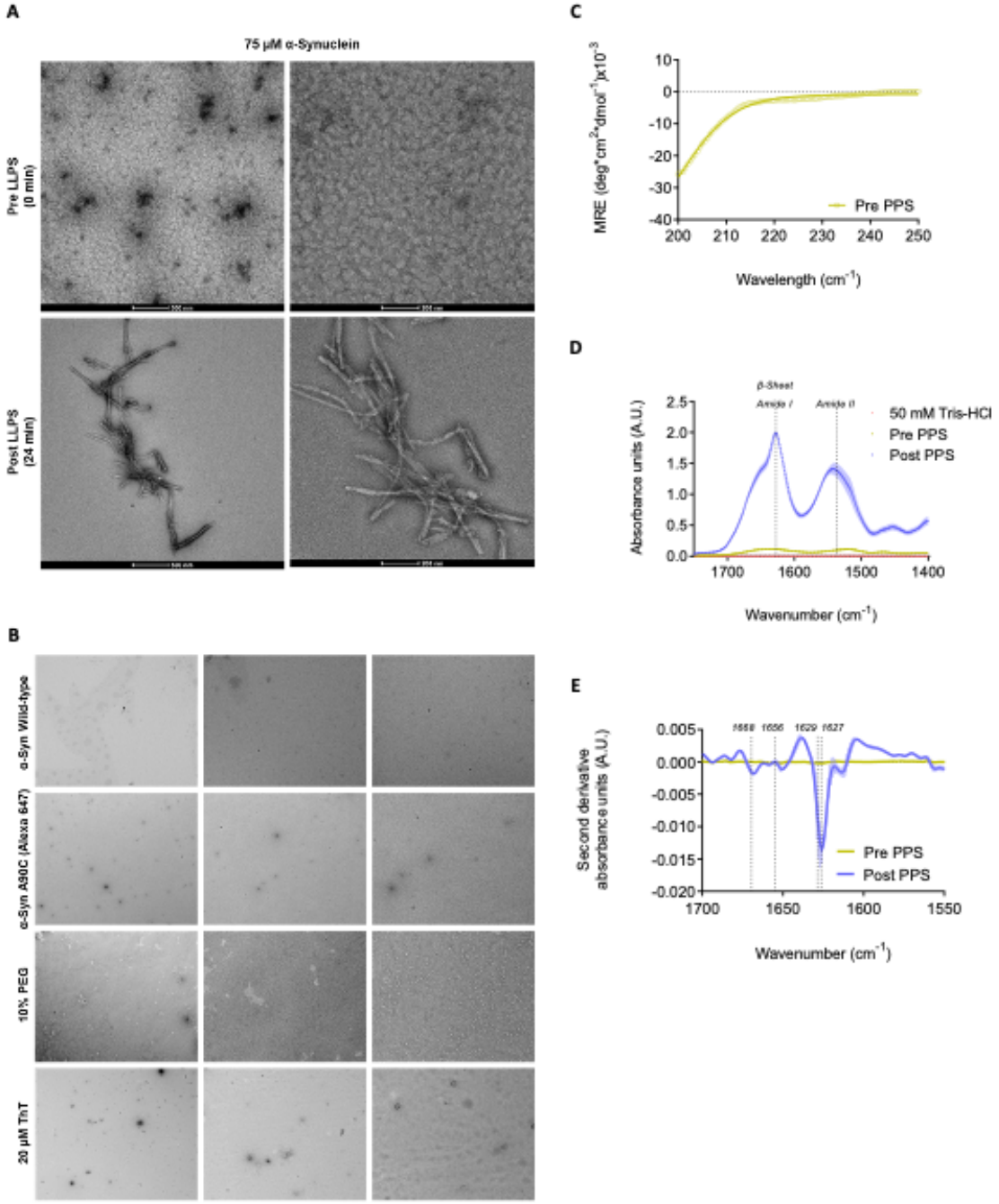


**Supplementary Figure 5. α-Synuclein condensates evolve into fibrillar aggregates over time. (A)** TEM images highlighting uranyl acetate α-synuclein species before (0 min) and after (24 min) phase separation. Monomeric species are highlighted at 0 min, whilst the formation of amyloid fibrils of α-synuclein post phase separation are validated at 24 min. Experiments were performed with 75 µM α-synuclein in 50 mM Tris-HCl, pH 7.4, 10% PEG and 20 µM ThT. **(B)** TEM images showing the absence of aggregates after 24 min of incubation with each individual component of the α-synuclein ThT aggregation assay through phase separation. 1700x, 5000x and 11500x direct magnification from left

to right panels were taken respectively. (**C)** Circular dichroism (CD) spectra confirming unfolded, random coil conformation of α-synuclein (75 μM) in solution, within the assay prior to phase separation. **(D)** Fourier-transform infrared (FTIR) spectra of 50 mM Tris-HCl (coral), sample pre-phase separation (yellow) and recovered products from phase separation assay (blue) (75 μM α-synuclein) highlighting the amide I and amide II regions. (**E)** Second derivative FTIR spectra of deconvoluted amide I region from panel F showing the band frequency assignments assigned to α-helix (~1656 $cm^{-1}$), β-sheet (~1627 $cm^{-1}$) and turn (~1668 $cm^{-1}$) structures pre (yellow) and post (blue) phase separation of α-synuclein (75 μM). Experiments were performed in 50 mM Tris-HCl at pH 7.4.

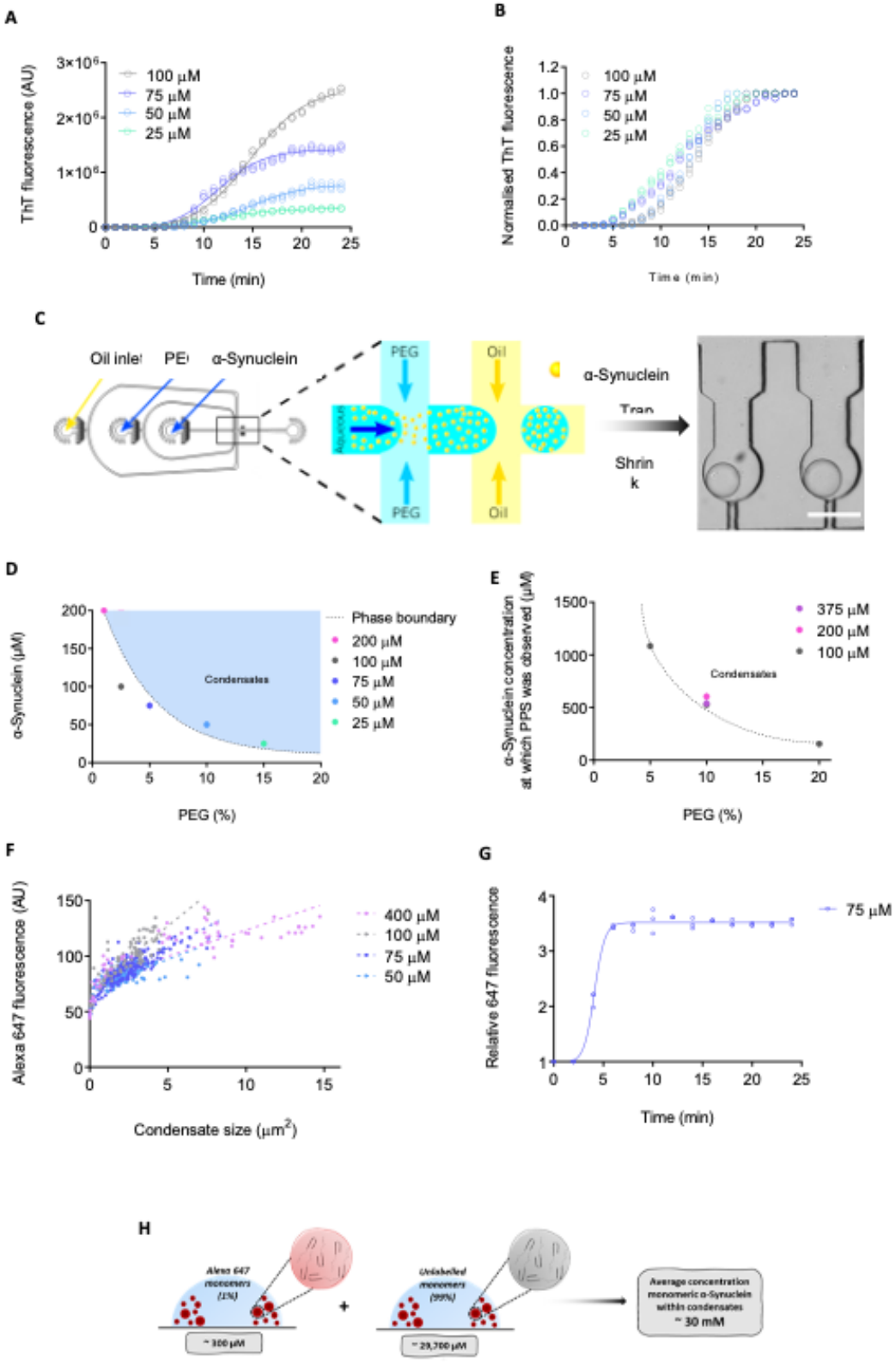


**Supplementary Figure 6. The concentration of α-synuclein required for phase separation depends on the type and concentration of the crowding agent used. (A,B)** Within condensates, normalised

aggregation data at four α-synuclein concentrations (100 (grey), 75 (blue), 50 (cyan) and 25 (turquoise) μM), yielded almost no variations between different concentrations. **(A)** Quantification of ThT emission over a 24 min period for the four different α-synuclein concentrations. **(B)** Normalised representative aggregation kinetic traces of α-synuclein shown in panel A. All experiments were performed in 50 mM Tris-HCl at pH 7.4 in the presence of 10% PEG and 20 μM ThT. **(C)** Schematic illustration of the microfluidic device used to obtain the concentration at which α-synuclein phase separation is observed. The device is pumped with oil, PEG and α-synuclein: (i) PEG and α-synuclein are mixed first to make droplets, and (ii) the droplets are then pushed and trapped in a chamber enclosed by fluorinated oil, for observation using microscopic techniques. The scale bar represents 100 μm. **(D)** Phase diagram showing the relationship between different α-synuclein concentrations, PEG concentration and the concentration at which phase separation is observed in the ThT-based assay with varying PEG and protein concentrations. An approximate phase boundary is represented by a black line. **(E)** Phase diagram showing the relationship between different α-synuclein concentrations, PEG concentration and the concentration at which phase separation is observed in the microfluidics-based assay with varying PEG and protein concentrations. A dotted black line is used for guidance as the trend follows the same trend shown in panel B. Values are detailed in **Supplementary Table 1. (F)** Scatter plot showing the relationship between condensate size and Alexa Fluor 647 fluorescence for individual condensates of 400 (light purple), 100 (grey), 75 (blue) and 50 (cyan) μM α-synuclein, 10 min from the onset of phase separation ($n > 70$ condensates per concentration); the linear regression coefficient $r^2$ is 0.63 for 400 μM, 0.71 for 100 μM, 0.70 for 75 μM and 0.44 for 50 μM. **(G)** Progression of Alexa Fluor 647 fluorescence intensity with time for α-synuclein (75 μM), which was measured at > 1 min and normalised against the first time point. After 5 min from the onset of phase separation, the Alexa Fluor 647 fluorescence intensity remains constant. **(H)** Estimated total α-synuclein concentration within condensates, which is approximately 30 mM; the total α-synuclein concentration (labelled and unlabelled) within condensates was estimated at an average of 33.5, 31.9, 28.4 and 25.8 mM for samples at 400, 100, 75 and 50 μM α-synuclein. Data are from a representative experiment that was repeated at least three times with similar results. All phase separation experiments were performed in 50 mM Tris-HCl, pH 7.4 and 10% PEG unless otherwise stated.

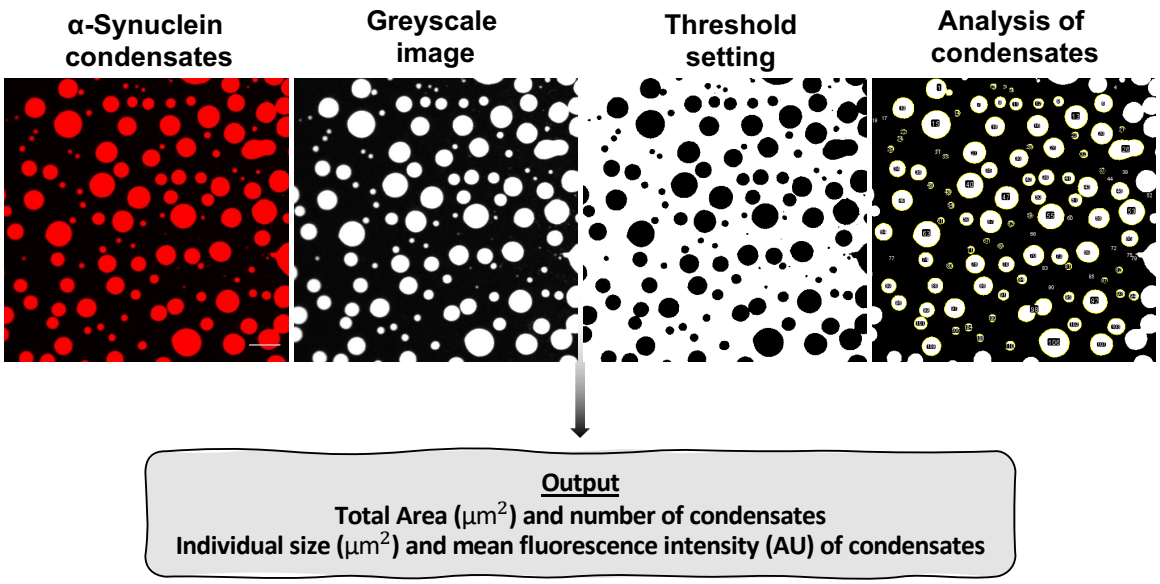


**Supplementary Figure 7. Fluorescence image analysis of α-synuclein condensates.** Images of wild-type α-synuclein, containing 1 molar % A90C α-synuclein labelled with Alexa Fluor 647 were acquired on a Leica TCS SP8 inverted confocal microscope system. All images within an experiment were acquired using identical confocal settings (scan speed, resolution, magnification, laser intensity, gain, and offset). Images were analysed by applying threshold functions in ImageJ software that identified the phase separated α-synuclein condensates and excluded the background of the image. All condensates within the threshold limits were analysed for total area ($\mu m^2$), number and average size of individual condensates ($\mu m^2$) and mean fluorescence intensity of individual condensates (arbitrary units). The scale bar represents 10 μm.

**Supplementary Table 1. Values of the concentrations of α-synuclein, ThT and PEG at which phase separation was observed in the microfluidics measurements described in this work.**

| α-Synuclein monomer concentration (μM) | PEG concentration (%) | α-Synuclein concentration at which LLPS was observed (μM) | Standard deviation (STD) | ThT concentration at which LLPS was observed (μM) | Standard deviation (STD) | PEG concentration at which LLPS was observed (%) | Standard deviation (STD) |
|---|---|---|---|---|---|---|---|
| **100** | **5** | 1084 | 10.8436 | 218.7182975 | 4.019814 | 54.21799085 | 1.380908 |
| **100** | **10** | 527 | 15.76637 | 78.62773753 | 3.153274 | 39.31386876 | 1.576637 |
| **100** | **20** | 154 | 4.012245 | 30.93155071 | 0.856264 | 30.85039194 | 0.802449 |
| **200** | **10** | 604 | 16.85452 | 65.0901998 | 6.164437 | 32.5450999 | 3.082218 |
| **375** | **10** | 538 | 13.03347 | 57.39246923 | 1.390237 | 28.69623462 | 0.695118 |

**Movie S1. Formation of α-synuclein condensates (75 µM) at the edge of a drop in 50 mM Tris, pH 7.4 and 10% PEG; the scale bar represents 20 µm.**

**Movie S2. Fusion events of several α-synuclein condensates after 7 min post the onset of phase separation; the scale bar represents 20 µm,**

**Movie S3. α-Synuclein condensates formation and maturation, and α-synuclein aggregation at near-physiological concentration (75 µM) and conditions (50 mM Tris, pH 7.4) in the presence of 20 µM ThT; Alexa 647 channel (red) ThT channel (green) and merged channels; the scale bar represents 10 µm.**

**Movie S4. Time-lapse of formation of α-synuclein condensates in droplets trapped within the microfluidic device.**

**Movie S5. 3D rendered composition from Z-stacked images showing preformed fibrils (Alexa Fluor 488 - green) co-localised with α-synuclein condensates (Alexa Fluor 647 - red).**

**Supplementary References**


1. G. Fusco *et al.*, Direct observation of the three regions in α-synuclein that determine its membrane-bound behaviour. *Nat. Comm.* **5**, 1-8 (2014).
2. Z. Toprakcioglu, P. K. Challa, A. Levin, T. P. Knowles, Observation of molecular self-assembly events in massively parallel microdroplet arrays. *Lab Chip* **18**, 3303-3309 (2018).
3. Z. Toprakcioglu *et al.*, Multi-scale microporous silica microcapsules from gas-in water-in oil emulsions. *Soft Matter* **16**, 3082-3087 (2020).
4. Z. Toprakcioglu, T. P. Knowles, Sequential storage and release of microdroplets. *Microsyst. Nanoeng.* **7**, 1-10 (2021).
5. C. Weber, T. Michaels, L. Mahadevan, Spatial control of irreversible protein aggregation. *eLife* **8**, e42315 (2019).
6. G. Meisl *et al.*, Molecular mechanisms of protein aggregation from global fitting of kinetic models. *Nat. Protoc.* **11**, 252-272 (2016).